

NASA TECHNICAL
MEMORANDUM



N73-31728
NASA TM X-2868

NASA TM X-2868

CASE FILE
COPY

A PRELIMINARY ANALYSIS OF
A RADAR-MAPPING MISSION TO VENUS

*by John S. MacKay, Larry E. Edsinger, Lawrence C. Evans,
Larry A. Manning, Kenneth F. Sinclair,
and Byron L. Swenson*

*Ames Research Center
Moffett Field, Calif. 94035*

1. Report No. NASA TM X-2868		2. Government Accession No.		3. Recipient's Catalog No.	
4. Title and Subtitle A PRELIMINARY ANALYSIS OF A RADAR-MAPPING MISSION TO VENUS				5. Report Date September 1973	
				6. Performing Organization Code	
7. Author(s) John S. MacKay, Larry E. Edsinger, Lawrence C. Evans, Larry A. Manning, Kenneth F. Sinclair, and Byron L. Swenson				8. Performing Organization Report No. A-4834	
				10. Work Unit No. 790-91-41-03-15	
9. Performing Organization Name and Address Ames Research Center Moffett Field, Calif. 94035				11. Contract or Grant No.	
				13. Type of Report and Period Covered Technical Memorandum	
12. Sponsoring Agency Name and Address National Aeronautics and Space Administration Washington, D. C. 20546				14. Sponsoring Agency Code	
15. Supplementary Notes					
16. Abstract This report presents a rather broad survey of the Venus radar orbiter possibilities within the period 1983-1990. Minimum mission imaging requirements have been set by comparison with the improving capabilities of Earth based radar systems and an examination of Earth airborne radar imaging. This has led to a requirement for 80 percent coverage at a resolution of 100 m. A first main conclusion is that only the Shuttle/Centaur launch system would be capable of establishing a circular orbit under all possible launch conditions. Thus, orbit eccentricity has been introduced as a parameter throughout this presentation. An examination of typical radar designs has led to upper and lower limits on swath width of 100 and 50 km. A lower eccentricity of ≈ 0.2 was set by considering the current Viking propulsion system. An examination of solar perturbations indicates that orbit maintenance problems increase rapidly above an eccentricity of 0.5. Having defined an area of interest in the swath width-eccentricity coordinates, a number of Venus approach mass estimates were made for cases within the established bounds. These indicated low mass values for high eccentricity designs. This was the result of the low retro velocity requirements of eccentric orbits. It therefore seems that moderately eccentric orbits are an interesting approach to Venus radar mapping. However, elliptic orbits extend the minimum mapping time from 120 to 240 days.					
17. Key Words (Suggested by Author(s)) Venus radar orbiter Imaging Mapping				18. Distribution Statement STAR Category: 30, 31	
19. Security Classif. (of this report) Unclassified		20. Security Classif. (of this page) Unclassified		21. No. of Pages 69	
				22. Price* \$3.00	

SYMBOLS

B	bandwidth, Hz
C	ion rocket exhaust velocity, km/sec
C_3	twice launch energy per unit mass, km ² /sec ²
c	speed of light, km/sec
D	antenna height, m
ERP	effective radiated power, dB
e	eccentricity
f	frequency, Hz
G	number of bits used in image gray scale
H	altitude, km
I_{sp}	specific impulse, sec
i	orbit inclination, deg
K	$4\pi kT \frac{S}{N} \frac{\ell(R)}{\sigma \eta^2}$
k	Boltzmann's constant, J/°K
L	antenna length, m
$\ell(R)$	loss function for radar equation
N	number of orbits between swaths
P	peak power, W
\bar{P}	average power, W
R	range, km
Δr	range resolution, m
$\frac{S}{N}$	signal-to-noise ratio
T	noise temperature, °K

t_o	integration time, sec
V	spacecraft velocity, km/sec
ΔV	retro velocity increment, km/sec
V_∞, VHP	spacecraft approach speed relative to Venus, km/sec
W	swath width, km
X, Y, Z	planet-centered coordinates defined in figure 7
ΔX	azimuth resolution, m
α	depression angle, deg
β	beam spread angle, deg
δ	declination of V_∞ vector at Earth or Venus, deg
ϵ	angle between planet approach hyperbola asymptote and periapsis direction, deg
η	antenna efficiency
Λ	latitude, deg
λ	wavelength, cm
μ	gravitational constant, km ³ /sec ²
σ	scattering coefficient
τ	pulse duration, sec
u	true anomaly, deg
ψ	incidence angle at planet
Ω	longitude of ascending node, deg
ω	argument of pericenter, deg

Subscripts

α	azimuth
p	periapsis
r	range
rf	radio frequency

A PRELIMINARY ANALYSIS OF A RADAR-MAPPING MISSION TO VENUS

John S. MacKay, Larry E. Edsinger, Lawrence C. Evans,
Larry A. Manning, Kenneth F. Sinclair, and Byron L. Swenson

Ames Research Center

SUMMARY

This report presents a rather broad survey of the Venus radar orbiter possibilities within the period 1983-1990. Initially, the detail of spacecraft design is reduced in order to expand consideration to all the opportunities within the entire period. This is done by considering only the radar imaging experiment and the subsystems needed to support it. This is justified by recognizing that the data transmission rates and RF power levels will be set by the requirements of such an experiment.

Minimum mission imaging requirements have been set by comparison with the improving capabilities of Earth based radar systems and an examination of the results of Earth airborne radar imaging. This has led to a requirement for high coverage (80 percent or greater) at a resolution of 100 m in both azimuth and range.

A first main conclusion is that only the Shuttle/Centaur launch system combined with a very large Earth storable retro propulsion system would be capable of establishing a circular orbit under all possible launch conditions. Thus, orbit eccentricity has been introduced as a parameter throughout this presentation.

An examination of typical radar design parameters has led to upper and lower limits on swath width of about 100 and 50 km. A lower limit on orbit eccentricity of ≈ 0.2 was set by considering the current Viking propulsion system. A separate examination of solar perturbations indicated that the orbit maintenance problem increases rapidly above an eccentricity of 0.5.

Having defined an area of interest in the swath width-eccentricity coordinates, a number of Venus approach mass estimates were made for cases within the established bounds. These indicated low mass values for high eccentricity designs. This was the result of the low retro velocity requirements of eccentric orbits.

It therefore would seem that the use of moderately eccentric orbits is an interesting approach to meeting the Venus radar mapping requirements. However, the use of elliptic orbits extends the minimum mission mapping time from 120 to 240 days. This creates a variety of lifetime related technology problems for many subsystems.

INTRODUCTION

Although Venus has been examined repeatedly from Earth and from flyby spacecraft, and although its atmosphere has been probed directly several times, very little is known of the physical history of Earth's nearest neighbor planet in the solar system. Since Venus is a terrestrial-type planet with size and mass nearly equal to those of Earth, there is considerable scientific interest in discovering the phenomena and processes that have shaped its surface. A detailed study of the morphology of the surface may provide new information on the formation of the solar system and new understanding of similar processes here on Earth.

Earth-based radar telescopes have recently succeeded in penetrating the continuous cloud cover of Venus to image some of the features of a small part of the total surface to a coarse scale. Such measurements can, however, only be made near inferior conjunction of Venus with Earth and the retrograde rotation of Venus about its axis is such as to always present the same hemisphere toward Earth at inferior conjunction. Thus complete surface coverage is not possible using Earth-based radar. For this reason and the poor resolution from Earth, a properly placed radar-mapping satellite in orbit about Venus could reveal important high and moderate resolution information concerning the topography of the surface over a nearly global scale. It is also possible that such a satellite could provide concomitant data on surface structure and composition. The purpose of the present report is to present a preliminary examination of the feasibility of placing such a satellite in orbit about Venus and retrieving the information.

To provide a basis for analyzing the feasibility of this mission, the science requirements are examined first. These requirements are developed from a rational relative to the surface exploration goals for Venus. A detailed analysis and discussion of the mission systems tradeoffs is then made. Finally, a specification of desirable mission operational profiles and spacecraft design options is presented and an assessment of the implied technology requirements made.

SCIENCE REQUIREMENTS

The primary scientific goals for the exploration of the surface of Venus, as delineated by the Space Science Board (ref. 1), toward which an orbiting radar-mapping mission would provide information are as follows: (1) determine the geometric shape of Venus, (2) examine the surface morphology, and (3) examine the crustal structure.

Mapping Data Requirements

On the basis of experience with optical imagery, the first goal requires regional coverage of surface elevations and average slopes with a horizontal resolution of about 1 km. A vertical resolution of perhaps 500 m is desired for at least 80 percent of the global surface. It should be noted that high surface area coverage does not require extensive latitude range. For example, 87-percent coverage results from $\sim 60^\circ$ latitude above and below the equator. To adequately examine surface morphology photographically requires a horizontal resolution of about 100 m with a vertical resolution of about 50 m on a local scale. These local areas could be selected from the lower resolution images and might represent a total coverage of at least 10 percent of the total global surface. The third goal, that of examining the detailed structure of crustal features, can, to some extent, be met with photographs having a ground resolution of 100 m, but it normally requires images with detailed resolution as small as 1 m. Such fine resolution is necessary only over very small areas, however, possibly less than 1 percent of the surface. A more detailed discussion of the scientific objectives for surface imagery of Venus has been given by Klopp et al. (ref. 2).

These resolution requirements are based on well-established, familiar photogrammetric techniques; some caution should therefore be used in interpreting them in terms of radar resolutions. These photogrammetric techniques have been developed and refined and have gained acceptance through a long history of interpreting aerial photography with "ground truth" corroboration and a shorter history of lunar and planetary imaging. Radar imaging techniques, on the other hand, do not have such an extensive historical basis. The possibility of nonmilitary applications of radar was first reported in 1948 (ref. 3), but it was not until the early 1960's that limited declassification of data concerning imagery generated by Side-Looking Airborne Radar (SLAR) systems allowed an open discussion of the geoscience potential of such imagery (refs. 4 and 5). Although the geoscience capabilities of SLAR imagery have been well documented in the last 10 years,¹ such imagery does not seem to have gained widespread familiarity among the community of geoscientists and planetologists, and its potentials are just beginning to be appreciated (ref. 7). A brief summary of the geological capabilities and requirements of radar imagery will aid in placing the resolution requirements mentioned above in perspective.

¹An extensive bibliography covering this documentation is not appropriate here. A bibliography covering most of the work prior to 1968 has been compiled by R. L. Waters (ref. 7); a list of more recent references is given by R. K. Moore (ref. 8). Other pertinent references will be cited as needed.

Spatial relationships are extremely important to the study of structural geology, and the representation of these relationships in radar images is very similar to the representation in aerial photographs. As a consequence, a great deal of information is available to the geologist from radar imagery. Reeves (ref. 8), for instance, has pointed out that some features, especially those associated with linearities (e.g., faults), are more easily identified on radar images than on comparable aerial photographs. One of the best illustrations of the type of information available is the SLAR imagery of eastern Panama taken by the U. S. Army Corps of Engineers (ref. 9) and interpreted at the University of Kansas by MacDonald (ref. 10) and Wing (refs. 11 and 12). This region is virtually inaccessible from the ground due to dense forests and hostile natives (Cuña Indians) (ref. 13) and has proved impossible to map with conventional aerial photography due to a virtually permanent cloud cover (ref. 8). Consequently, the interpretation of the radar imagery was done a priori; it was not biased by a preknowledge of the existing geological features.

Most of these radar images have a nominal ground-resolved distance of ~15 m; examples of this imagery, which were kindly provided by L. F. Dellwig, R. K. Moore, and R. S. Wing of the University of Kansas, are shown in figures 1(a) and 2(a). On the basis of a series of such radar images, Wing was able to identify numerous previously unknown examples of the following types of structural-physiographic elements: features related to folded strata, such as anticlines and synclines; fault-related features, such as faults, contacts, grabens and horsts; and igneous features, such as dikes, plugs, domes, and calderas. He was also able to identify major strata and blocks and measure dips and strikes. Figures 1 and 2 show examples of some of these features. The net result of the SLAR imagery interpretations of MacDonald and of Wing is the geological reconnaissance map of Panama shown in figure 3 (reproduced with permission from ref. 10). This is a graphic example of the wealth of structural geologic information available from radar imagery alone. For comparison, figures 1(b) and 2(b) also include the same imagery systematically degraded to simulate a resolution of ~100 m.

It would appear then that the resolutions specified above for optical photographs can be directly interpreted in terms of ground-resolved distances on radar images. There are, however, several other facets of radar imagery which must be considered in designing a planetary radar-mapping mission; the most pertinent of these are stereoscopic imaging, multispectral imaging, and polarization.

"Stereoscopic" imaging—Experience in aerial photography has indicated that the increase in usefulness gained by generating stereo photographic images is far out of proportion to the attendant increase in effort required. This is undoubtedly due, at least in part, to the remarkable efficiency of the human brain in interpreting stereo-optical images in terms of three-dimensional configurations. The advantages of using this interpretive ability are not available, however, in the case of radar imagery due to fundamental differences in the imaging process.

Nevertheless, it has been conclusively demonstrated that a comprehensive interpretation of radar imagery almost requires imaging from more than one direction (refs. 8, 10, and 14). At Venus, some shadowing ambiguities and the heights of some objects could be resolved by requiring >50 percent overlap between adjacent swaths, thus ensuring that the entire surface is seen from two directions. On the other hand, studies of geological structures in Panama with SLAR imagery (refs. 10 and 14) have shown that linear features can be completely suppressed if they make an angle of $\leq 30^\circ$ with the viewing direction. There is a strong argument, therefore, for attempting to obtain imagery from four orthogonal look directions. Combined with a >50-percent swath overlap, this could be achieved in at least two ways: (1) using two spacecraft with orthogonal orbit inclinations or (2) operating a single spacecraft in a "squint" mode whereby the radar beam is alternately directed 45° forward and 45° backward along the flight path, with the corresponding images recorded separately. The former method would provide four-direction imagery for at least some fraction of the surface, while the latter technique would provide such imagery for the entire coverage of the spacecraft.

"Multispectral" imaging—Mapping with multifrequency radar systems is somewhat of a microwave equivalent of multiband spectral reconnaissance in optical wavelengths using very narrow bandwidths. To date, very little field work has been done to investigate the advantages of such radar systems, but such studies as have been done indicate that imaging at multiple frequencies may be more of an advantage in radar reconnaissance than in optical reconnaissance. One of the principal advantages in color photography is the increased interpretation efficiency, while one of the main advantages of multifrequency radar imagery is related to the surface penetration of the radiation. In a controlled experiment to measure the surface penetration of radar, Badgley and Lyon (ref. 15) placed a reflecting surface at the bottom of a sample of dry (~17-percent H₂O) sand and systematically removed layers until a signal was detected at normal incidence. As one would expect, they found a strong frequency dependence, with X-band signals ($\lambda \approx 3.5$ cm) penetrating ~5 cm of sand, C-band ($\lambda \approx 5.5$ cm) penetrating ~20 cm, and P-band ($\lambda \approx 133$ cm) penetrating to a depth of more than 800 cm.

One of the implications of this study is that multifrequency radar imagery might be able to be used to detect subsurface layering. This implication has been shown to be valid in radar imaging studies of the Pissgah Crater area of California (ref. 16). In this area, there are extensive lava flows, some of which have been covered by windblown sand. Dellwig found that K-band ($\lambda \approx 2$ cm) images showed the sand and the lava flows where the latter were free of sand, while P-band signals ($\lambda \approx 70$ cm) penetrated up to 180 cm of sand to accurately portray the underlying lava flows. Considering the hot, dry conditions expected at the surface of Venus (ref. 17), the sensitivity of dual-band imagery in the detection of aeolian layering of dry sand, which has been expressly demonstrated by these two studies, is very pertinent.

The frequency selection tradeoffs will be discussed in more detail below; it would appear that atmospheric attenuation may restrict the system to wavelengths ≥ 3 cm (X-band), while the low-frequency limit will be primarily determined by spacecraft considerations.

As in the case of "stereo" imaging, although the prospects of the additional information available from multiple frequency imaging are exciting, the baseline mission involving a single frequency will yield a great deal of scientifically interesting information.

Polarization—Most SLAR systems were initially designed to image only the component of the return signal which was polarized in the same direction as the illuminating beam. There have been several examples recently, however, of important results being obtained from the cross-polarized image which were impossible from the like-polarized image (refs. 20 to 25). Perhaps the most striking example involved another study of the lava flows in the Pissgah Crater area in which a comparison between the like- and cross-polarized images allowed the separation of lava flows of different ages, weathering, and roughness (refs. 21 and 22). The availability of images from both polarizations seems essential to the complete identification of features and may also allow the identification of mineralogy (ref. 26). It is not clear, however, how the advantages of having both types of images is affected by resolution or by the influence of moisture content on the enhancement of the cross-polarized image. It may be true that the cross-polarized signal is highly dependent on the amount of moisture in the surface, thus accounting for the relative difference in returns from different rock types and across faults (ref. 26). If the depolarization of the signal is indeed strongly dependent on the moisture content of the target, then the usefulness of dual polarization imagery of the surface of Venus would be speculative due to the expected absence of liquid water (ref. 17 and others).

Earth-Based Capability

Before examining the capability to achieve the desired images and coverage from an orbiter, it is only proper to inquire into the achievements and capability of Earth-based radar systems. During the inferior conjunction of 1969, radar maps of the surface of Venus were obtained with the 36-m Haystack and 18-m Westford antennas (ref. 28), the 64-m Goldstone antenna (ref. 29), and the 296-m Arecibo antenna (ref. 30). The resultant map generated from the Goldstone data is shown in figure 4. This image has a horizontal resolution of about 80 km and covers a region of latitude from about 10° to 40° both north and south over nearly one hemisphere of the planet. Unfortunately, the resolution degrades rapidly as the distance between Earth and Venus increases. In addition, the slow retrograde rotation of Venus about its axis is locked with the rotation of Earth about the Sun so as to always present the same face toward Earth at inferior conjunction. Thus, only one hemisphere of Venus can effectively be imaged by a signal from Earth.

Several interesting large features have been noted even at this coarse resolution. Improvements can be made in the imaging technique and are planned for future conjunction periods. Use of these improvements and the large 296-m antenna at Arecibo may result in images with resolutions approaching 2 km. Again, however, this resolution will be confined to part of a single hemisphere. The next most favorable observational periods during which Arecibo can view Venus at inferior conjunction are 1980, 1988, and 1996. The resolution achievable in these three conjunctions is shown in figure 5 as a function of the longitude on the surface of Venus. The best values of resolution occur at the point of closest approach (conjunction) between the planets and degrades at other points due to the increased distance before and after conjunctions. If the desired resolution within the swath is approximately 2 km or less, then coverage from 10° to 32° latitude is possible. If a lower resolution is considered, then coverage up to 70° latitude becomes possible at about 5 km resolution.

Although the images implied by figure 5 are going to have significant scientific value and are well worth making, they will not satisfy the basic requirements for a good understanding of the morphology of the surface of Venus. They can, if made in 1980, provide an excellent basis for the preliminary planning for the localized 100-m coverage by an orbiter.

MISSION AND SYSTEMS ANALYSIS

The choice of the appropriate mission and systems design of an orbital radar mapper of Venus is much more interactive than most other unmanned exploration missions. There are strong interactions between the resolution and coverage requirements on one hand and the selection of the heliocentric transfer and planetary mapping orbits on the other. These choices also effect the selection of alternatives for the radar antenna, attitude control, power, data handling, communications, and retro propulsion subsystems. In this section, the requirements for heliocentric transfer to Venus and for orbital insertion into an orbit about Venus will be discussed. This will have resulting implications on the swath width of the imaging strips which, in turn, will have strong implications on the size of the radar antenna and the associated power requirements to illuminate that area. Finally, the level of these power requirements has strong implications on the power system choice and the orbital operations for mapping and communication of the mapping data back to Earth.

Heliocentric Trajectories

The conditions for departure from Earth and arrival at Venus (ref. 35) are shown in figures 6(a) through (j) for each of the five launch opportunities in the 1980's (i.e., 1983, 1985, 1986, 1988, and 1990). Two figures are shown for each launch opportunity. The first gives contours of departure injection energy C_3 and declination as a function of departure and arrival dates. The departure and arrival dates are given as Julian calendar

dates and both type I (heliocentric transfer angles less than 180°) and type II (heliocentric transfer angles greater than 180°) trajectories are shown. The second figure in each pair gives similar contours of arrival hyperbolic excess speed at Venus, V_∞ , and the declination and right ascension of the approach hyperbolic asymptote vector. Declination and right ascension are defined in a planet-centered inertial coordinate system with the positive X-axis parallel to the major axis of Venus and in the direction of perihelion. In this coordinate system, the Z-axis is normal to the Venus orbit plane and in the direction of the rotation vector of Venus about the Sun. The rotation of the surface of Venus relative to this coordinate system is retrograde. For the purposes of this study, the equator of Venus is assumed to coincide with the Venus orbit plane. A typical set of Venus arrival conditions relative to this coordinate system is shown in figure 7.

Orbit Insertion Requirements

The arrival hyperbolic excess speed and orbit eccentricity chosen determine the insertion impulse required to achieve that orbit. It can be seen from figures 6 that the typical range of excess speed is between 4 and 6 km/sec. The required impulsive velocity, ΔV , for insertion into orbits of various eccentricities is shown in figure 8 for a range of hyperbolic excess speeds between 4 and 6 km/sec. For these curves, a periapsis altitude of 500 km was assumed. It can be seen that the ΔV requirement to insert into a circular orbit lies between about 3.5 and 4.5 km/sec. Such a high requirement implies a space storable insertion stage. Earth storable propellants just do not have sufficient specific impulse to deliver such a high ΔV to typical orbiter payloads. Furthermore, with space storable propellants having a specific impulse of, say, 385 sec, less than one-third of the weight approaching Venus can be placed into a circular orbit about Venus. Thus it appears highly desirable to consider eccentric orbits in order to take advantage of the associated decrease in insertion requirements.

To achieve the maximum area coverage of the planet with a single spacecraft, a high inclination orbit is required, and periapsis should be placed over the equator. (Other periapsis positions would create redundant coverage above or below the equator.) Full longitudinal coverage is then obtained through the very slow rotation of the planet under the inertially fixed orbit plane. It is not generally possible to establish a polar orbit with periapsis over the equator using an optimum insertion at the periapsis of the approach hyperbola. Thus a penalty for periapsis rotation must be added to the values shown in figure 8. The total insertion velocity requirement is shown in figures 9(a) to (c) as a function of the required periapsis rotation for several values of orbit eccentricity. Three values of V_∞ (4, 5, and 6 km/sec) are shown by the three figures.

The amount of periapsis rotation required to place the periapsis of a polar orbit at the equator is a function of arrival declination, arrival hyperbolic excess speed, and periapsis altitude. The angle between the approach asymptote and direction of periapsis of the approach hyperbola, ϵ , varies with V_∞ in the range of interest (as shown in fig. 10) for a 500-km

periapsis altitude. For absolute values of the arrival declination, δ , less than ϵ , the required periapsis rotation for polar orbits is always positive and is $\epsilon - |\delta|$. It can be seen from figures 6 that the arrival declination generally does not exceed $\pm 40^\circ$, thus satisfying the above condition that $|\delta| < \epsilon$. Given the desired orbital eccentricity and the periapsis rotation from the above computation, the optimal total insertion ΔV can be obtained from figure 9.

Launch Vehicle Capability

There are two potential launch vehicles that provide ejected payload masses in the range of interest for this mission. They are the planned space shuttle and Titan IIID topped by the Centaur stage. The Titan IIID version, modified to accept the Centaur upper stage, is now called the Titan IIIE in Lewis Research Center reports. The payload capability injected into an interplanetary trajectory for these two launch systems is shown in figure 11(a) as a function of the departure orbit energy, C_3 . The addition of a third stage (e.g., the TE-364-4) to the launch vehicle combination does not become effective until C_3 values of over 50 are required. Reference to figures 6 shows that such values are not necessary for this mission. The seven-segment Titan/Centaur combination, if developed, would provide a capability midway between those shown.

If the launch vehicles are to leave the Cape Kennedy launch facility, then the launch azimuth will be restricted to be between approximately 44° and 114° where 90° (measured from due north) represents a due east launch. If the declination of the departure conic asymptote exceeds the orbit inclinations possible from the launch site, then a dogleg or plane change maneuver is required of the launch vehicle. This will reduce the payload considerably below those shown in figure 11(a). This problem has been investigated for the Titan IIIE/Centaur launch vehicle departing from Cape Kennedy with a launch energy $C_3 = 10 \text{ km}^2/\text{sec}^2$. The results are given in figure 11(b), which shows the possible departure declinations as a function of the orbital coast time required of the Centaur stage. Also shown is a band containing launch azimuths between the limits of 44° and 114° . An examination of the launch opportunities contained in figures 6 shows that a worst case occurs in 1988 (fig. 6(g)) having a departure declination of, at most, 50° . From figure 11(b), this declination is possible for coast periods of approximately 1 hour and launch azimuth slightly below 114° . It therefore appears that no launch azimuth problems exist for the range of selected launch dates unless Centaur orbital coast periods of at least 1 hour are not achieved by the late 1980's.

Orbit Selection

At this point, it is possible to select approach velocities at Venus which are representative of the time period under consideration (1983 to 1990). Also, using the launch vehicle performance curves (fig. 11(a)), a range of planet approach masses can be estimated from the C_3 information

shown in figures 6. For any given propulsion system and payload, it then becomes possible to establish a range of orbit eccentricities within the capabilities of selected systems.

Estimated spacecraft masses can be obtained from Brown, Elachi, Jordan, Laderman, and Thompson (ref. 31) and Brandenburg and Spadoni (ref. 33). These are studies of near-circular mapping orbits (using either solar cell or RTG power systems), and the masses presented can, for that reason, probably be regarded as minimum values. From Scofield (ref. 34), the details of the Viking propulsion system have been selected as typical of current technology. Two different propellant loadings have been examined for this system: one using the planned value for the Viking mission and the other using that for a mission to the moons of Mars.

The factors and options just described are illustrated in figure 12(a), where velocity change required to establish a given orbit (with and without periapsis rotation) is plotted as a function of orbit eccentricity. Superimposed on this graph are the capabilities of the Titan IIIE/Centaur and Shuttle/Centaur launch vehicles used with a Viking propulsion system and with assumed spacecraft masses between 600 and 740 kg. This particular figure has been developed for a V_{∞} band between 3.5 and 5.5 km/sec and $C_3 = 10 \text{ km}^2/\text{sec}^2$, which represent typical cases for the 1983 to 1990 time period. These values include allowance for a 15-day launch window. The uppermost horizontal bands correspond to the capability of the Shuttle/Centaur and Titan IIIE/Centaur with a maximum bipropellant capability using the Viking system propellants and hardware weights without tankage dimensional limits. The two lower horizontal bands represent the two Viking system propellant loadings discussed by Scofield (ref. 34) as applied to the selected payloads between 600 and 740 kg.

From this figure, it is clear that the bipropellant Viking propulsion system must be considered with orbit eccentricities above 0.3 unless spacecraft masses considerably below 600 kg (the upper part of each horizontal band) appear feasible. The extended Viking, on the other hand, can be used for orbit eccentricities between about 0.2 and 0.5, depending on the launch year and periapsis location. For maximum bipropellant loadings, which depend on the launch vehicle chosen, it would appear that only the Shuttle/Centaur could achieve circular orbits over a wide range of launch conditions. For circular orbits, however, the retro propulsion system plus its propellant become the dominant part of the system, comprising better than 80 percent of the planet approach mass for the maximum bipropellant, Titan IIIE/Centaur case. Rather than carry such large amounts of propellant, it is probably more beneficial to consider the development of a space storable propulsion system that could have a specific impulse of 385 sec or higher. This would reduce the propulsion system to at most 70 percent of the approach mass and could allow the consideration of two separate spacecraft in a single shuttle launch. Furthermore, the development of a space storable stage could be of benefit to other future missions using the Shuttle/Centaur combination.

The alternative approach of designing the spacecraft for elliptical orbits at Venus will complicate the radar and attitude control system designs

and will require more power to compensate for the higher orbit altitudes. More serious, however, is the loss of coverage for higher eccentricities (no mapping near apoapsis), which can double the mapping time from 120 to 240 days. It is therefore important that the spacecraft implications of eccentric orbits be evaluated so that some comparison can be made with the circular orbit approach and its associated large retro propulsion requirements. This report will illustrate some of the spacecraft design options for eccentric orbits. For example, the tandem two spacecraft launch possibility is probably possible with the Shuttle/Centaur launch vehicle without the need for a space storable propulsion system development.

Figure 12(a) contains no information about a possible upper limit on orbit eccentricity. To better define this upper bound, a number of orbit maintenance calculations were made for polar orbits using the same set of launch and arrival dates chosen for figure 12(a). The propulsive velocity changes required to maintain the periapsis altitude within ± 50 and ± 100 km are shown in figure 12(b) as a function of orbit eccentricity. This figure has been developed for the 1983 launch opportunity and employs no periapsis rotation. All orbits are polar and initially have a 500-km periapsis altitude.

These data illustrate two distinct features about the effect of eccentricity and maintenance tolerances. First, a smaller tolerance increases the number of corrections required but reduces the size of the correction. Thus, the total sum of the corrections remains essentially the same within the range covered. Secondly, it appears that the required corrections vanish at eccentricities below about 0.50.

The data shown in figure 12(b) have been generated by numerical integration of the three-body equations of motion. The results have been verified by comparison with other n -body and special perturbation computer programs.

The effect of other launch periods and periapsis rotation has also been crudely evaluated. For example, other launch periods do not appear to alter results. This was verified by a check of the 1988 opportunity. Also, placing the periapsis over the equator by periapsis rotation reduces the corrections to zero at $e = 0.80$. However, such an orbit requires increased retro propulsion requirements.

Solar Electric Propulsion

As one of the spacecraft design options, the possibility of using a solar electric propulsion system, primarily for the retro maneuver, was considered. This is motivated by the possible dual use of the power system (e.g., for propulsion and for high-resolution radar mapping).

In the case of solar electric propulsion (SEP), it is usual to represent the mission capability by displaying the net or delivered spacecraft mass exclusive of the propulsion system power supply or thruster subsystems. This

practice will be continued here but will be done in such a way as to make it easy for the reader to add in the power supply mass if desired.

The effects of Venus capture orbit eccentricity and SEP power level (at Earth departure) are shown in figure 13 in terms of the net mass delivered (as described above). This particular case is for a 1983 opportunity and uses the Titan IIIE/Centaur launch vehicle for departure and an Earth storable type retro stage for the retro maneuver. The electric power is decelerated into orbit and is also used to reduce, via electric propulsion, the approach velocity (indicated on the figure) at Venus arrival. The ballistic approach speed in this case would normally be 3.0 km/sec. From this figure, it is evident that the main effect of the SEP system is to make available to the payload a wide variety of power levels without loss of spacecraft mass available for science or radar experiments. Also shown in this figure are the approach speed achieved and ion exhaust velocities required to produce the highest net mass. These are primarily a function of power level as indicated by the vertical dash lines.

One problem apparent from figure 13 is the low value of ion exhaust velocity (C) associated with the lower power levels. This occurs because the optimal value is lowered in an effort to gain the spacecraft acceleration needed to accomplish the proper heliocentric transfer. Electrostatic thrusters with such low values of C are not a well-developed technology at this time (e.g., the SERT II C value was approximately 42 km/sec). However, this problem can be alleviated by adjusting some of the other mission parameters as shown in figure 14. Here, the best value of C and the net spacecraft mass are shown as functions of the departure and arrival speeds (relative to Earth and Venus) for a power level of 5 kW at Earth. This figure shows that a small change, perhaps only 0.5 km/sec, in the departure and arrival speeds can be made to accommodate any desired or available thruster technology.

Low thrust capture— In the results discussed so far, the retro maneuver has been accomplished by a combination of SEP stage and an Earth storable retro stage. Another obvious option would be to use the SEP system for the entire retro maneuver. This option has been examined and the results of a typical case are shown in figure 15. Here, the net mass is shown as a function of the total trip time, including the time needed to establish the orbit at Venus, for a 15-kW (at Earth) SEP system. The orbit chosen in this instance is a circular orbit at an altitude of 1000 km above the surface of Venus. This is an extreme case (elliptic orbits require less spiral time) but shows that the trip time can become much longer than the 150 days shown previously before the net mass returns to the 1000 kg level. This is due to the time required to establish the orbit with the low thrust system. Also, it was found that power levels higher than before are much more necessary. On the basis of these considerations (longer time and the higher cost implied by the higher power levels), it was decided that the Earth storable retro approach was preferable.

Solar array limitations— Returning to the space storable retro case, it appeared that large amounts of power, up to 15 kW or higher, could be

accommodated. However, such arrays can be rather large, perhaps leading to structural problems during the retro maneuver. This problem has been given some preliminary consideration for a typical SEP stage design taken from reference 36. This particular case was a nominal 15-kW multipurpose stage and rollup array that is deployed by extending a central tabular metallic tape in two directions. The acceleration levels this particular design can withstand before the yield stress is reached is shown in figure 16 as a function of the power level. Also shown are the approximate dimensions of the tape tubes and the array in a 5-kW configuration. Different power levels are attained by extending the 4-m wide array to greater lengths. This figure illustrates that the arrays apparently have sufficient strength to endure typical rocket thrust accelerations, particularly at the lower power levels.

Launch window considerations— Another feature that an SEP system could offer is an extended launch window. This is illustrated in figure 17, where the net mass is shown as a function of time before and after the desired launch date. Shown here are data for an intermediate eccentricity of 0.5 with a periapsis altitude of 1000 km. The solid curves are for the high thrust case, while the dashed curves are for the SEP stage. The two curves shown for the SEP cases indicate the effect of including the mass of the solar arrays into the net mass delivered. Two observations are apparent from this figure:

- (1) The SEP approach does not give a large increase in delivered mass over the high thrust alternatives.
- (2) While the SEP approach widens the launch window considerably, there does not appear to be a serious launch window problem for the high thrust method.

An attempt was also made to significantly alter the Venus approach conditions through application of SEP thrust and flight time changes. This effort was abandoned once it became apparent that it could not be done without large decreases in the delivered mass. The hope had been that two separate spacecraft orbits could be established with a large angle between their major axes.

Summary— Based on the preliminary analysis made here, it does not appear that an SEP spacecraft or spacecraft/stage has any outstanding advantages for a Venus radar mapping mission. This is in agreement with the results of Brandenburg and Spadoni (ref. 33). This is due mainly to the fact that the Earth-to-Venus transfer is a low-energy mission. Thus, a reduction of the Venus approach speed, which is the main effect of the SEP operation, does not substantially reduce the retro maneuver energy required at Venus. Rather, the retro maneuvers depend almost entirely on the eccentricity of the desired orbit at Venus. Establishing the orbit at Venus using the SEP thrust was also investigated but required long periods of time (up to 50 additional days for a circular orbit) and increased solar cell power.

One apparent advantage for the SEP system is the ability to deliver a wide range of power levels with little or no reduction in the mass available

for other spacecraft functions or science instruments. Should there develop a need for power levels up to 20 kW in Venus orbit, then an SEP system would be given more detailed consideration.

Swath Width

One of the most important mission operation parameters is the swath width swept out by the radar beam as the spacecraft orbits the planet. It directly affects the amount of area coverage obtained and the power required. Also, together with the planet's rotation and mapping sequence strategy, it controls the degree of coverage overlap from swath to swath.

The factors that contribute to the determination of the swath width are illustrated in figure 18(a). From this figure it can be seen that the depression angle, α , altitude, H , and the range beamwidth, β_r , are all factors that affect the swath width, W .

Certain facts are evident from figure 18(a). First, the depression angle, α , cannot be so small as to let the beam go off the horizon of the planet; thus it must be greater than α_{\min} :

$$\alpha \geq \alpha_{\min} = \cos^{-1} \frac{1}{1 + (H/R)} \quad (1)$$

However, α is normally set at some value between α_{\min} and $\pi/2$ for a variety of other reasons. At small values of α , the beam passes through more atmosphere and also reflects back a much reduced part of the incident beam to the antenna. At the other extreme ($\alpha = \pi/2$), the range resolution is degraded and the swath width and coverage reduced if the antenna height is fixed.

Another factor affecting the choice of depression angle is the orbit selection. For high eccentricity orbits, the altitude will change in time and the beam will eventually rise above the planetary horizon (see eq. (2)). Thus, as indicated in figure 19, the fraction of the planet covered can drop off rapidly as the orbit eccentricity increases. This is particularly true for low values of depression angle as illustrated in the case of $\alpha = 30^\circ$.

However, while the coverage can be adequate for such cases as $\alpha = 60^\circ$, the slant range can become very large at the point at which the beam begins to leave the planet's surface. This can lead to high radar power requirements (as will be shown later). The conditions at which this occurs are determined from the relations:

$$H = R \left(\frac{1 - \cos \alpha}{\cos \alpha} \right) \quad (2)$$

and

$$R + H = \frac{(1 + e)(R + H_p)}{1 + e \cos v_{\max}} \quad (3)$$

Thus

$$v_{\max} = \cos^{-1} \left[\frac{(1 + e)(R + H_p) - (R + H)}{e(R + H)} \right] \quad (4)$$

where

v_{\max} maximum true anomaly of orbit
 H_p periapsis altitude
 e orbit eccentricity

In the special case where the periapsis of a polar orbit is over the planet's equator, v_{\max} is the maximum latitude north and south of the equator for which coverage is possible.

One method of avoiding the high powers associated with high values of α and concomitant slant range is to terminate mapping at some point prior to planet limb encounter. The effects of terminating the mapping when $H/H_p \leq 3$ are also shown in figure 19.

Figure 18(b) shows a simplified enlargement of the upper portion of figure 18(a). In particular, the curvature of the planet is ignored; the figure therefore applies to high values of α and near periapsis. Near the upper or lower end of the swath, the curvature of the planet may have to be included. From this figure, the following simple relationship can be derived:

$$\sin \beta_r = \frac{W \sin(\alpha + \beta_r)}{H} \sin \alpha \quad (5)$$

More exact relations, which apply over the entire swath, have been given by Klopp et al. (ref. 2, p. 234, vol. IV). However, equation (5) expresses the dominant interactions between the variables of interest. Thus, for given values of α , H , and W , a value of β_r can be determined. In the next section, the relation between β_r and antenna height, D , will be discussed.

Antenna Size

The antenna height, D , is related to the antenna range beam width by

$$\beta_r = \frac{1.25\lambda}{D} \quad (6)$$

Typical values of D and λ are 2 m and 15 cm, respectively. Thus it is clear that β_r will probably be rather small ($\approx 5^\circ$) so that equation (5) can be further simplified to

$$\beta_r \approx \frac{W \sin^2 \alpha}{H} \quad (7)$$

The choice of wavelength, λ , in equation (6) is limited by atmospheric absorption at the lower end and, for a given swath width, by the antenna height at the upper end. In some cases, it may occur that the antenna height that produces the desired swath width is much too large for standard spacecraft size and packaging dimensions. In such cases, it may be necessary to illuminate a much larger swath than is actually processed by the antenna. This is wasteful of power but prevents the problems of handling an unwieldy antenna. For this study, the antenna was limited to 2 m in height.

The determination of antenna length is much more complicated because it involves the interaction between the real antenna length, which sets the ground footprint illuminated by each pulse, and the synthetic antenna length, which is generated by the motion of the real antenna along the spacecraft trajectory.

The azimuth beam angle, β_a , is found from the antenna length, L , as in equation (6):

$$\beta_a = \frac{1.25\lambda}{L} \quad (8)$$

Thus the ground footprint is set by β_a , β_r , and α . However, the same antenna can receive many pulse returns from a given point on the surface as it moves along its path. If these returns are properly phased and combined, it will appear that the receiving antenna is much longer than it actually is. The various different points within the footprint can be identified in range by using the time of the returns and in azimuth by using the doppler frequency shift caused by the relative line-of-sight velocity between the ground and the moving antenna. The length of this synthetic antenna is therefore equal to the physical length of the footprint in the azimuth direction at each range.

In order that there be no ambiguity in the range information, each pulse must clear the swath before the next one enters. This sets the following

limit on the pulse repetition frequency (PRF):

$$PRF \leq c/2W \cos \alpha \quad (\text{see fig. 18(b)}) \quad (9)$$

For the given swath width and depression angle, equation (9) then represents an upper limit on PRF . Another limit is set by the requirement that there be no ambiguous returns in the azimuth information. This is expressed by:

$$\frac{4V}{PRF} \leq L \quad (10)$$

This relation, which is also used by Klopp et al. (ref. 2), places the side lobes of the synthetic antenna outside the main lobe of the real antenna. Compared to another relation frequently used (see ref. 32), equation (10) incorporates an additional factor of 2 to ensure that the synthetic antenna side lobes are well outside the real antenna main lobe.

Since there can be only one value of PRF , equations (9) and (10) can be equated, giving

$$L = \frac{8VW \cos \alpha}{c} \quad (11)$$

This gives a value for L which depends on periapsis altitude, depression angle, swath width, and spacecraft velocity.

Typical values of antenna height and length are shown in figure 20 as a function of orbit eccentricity. These values are for a wavelength of 13 cm and two different depression angles. Also shown is the effect of limiting the altitude rise to $H \leq 3H_p$. These values of antenna length are based on the periapsis velocity and are therefore long enough to account for the highest velocity within the swath. For elliptic orbits, the angle ψ (see fig. 18(a)) will eventually deviate significantly from α and approach zero. Referring to equation (11), it can be seen that, for $\alpha \approx 60^\circ$, L can be up to twice as long if it is sized for the limb runoff condition. Thus the antenna lengths shown are simultaneously sized for the highest velocity and smallest value of ψ within the swath. The swath widths associated with the antenna value shown in figure 20 are included in figure 21. These depend on the number of orbits, N , between successive swaths and the percentage overlap desired. In figures 20 and 21, $N = 1$ and the overlap is 20 percent.

From figure 20, it is clear that the antenna dimensions can become impractical, particularly when $\alpha \leq 30^\circ$. At very high eccentricities, the required antenna becomes both very long and very narrow. In this case the antenna height is approaching the wavelength, and it may become difficult to construct such an antenna and maintain predictable beam characteristics.

The only other constraint on antenna length is due to the minimum resolution possible, that is,

$$\Delta X = L/2 \quad (12)$$

However, this represents the best possible case and requires that all the information in the footprint be utilized. This implies a fully focused synthetic aperture system and may lead to unacceptable data rates. For elliptic orbits, the swath width will increase as the spacecraft moves away from periaapsis. Eventually, it would become difficult to process all the data in the beam footprint at the same resolution. Also, it may be prudent to illuminate a larger area than processed in order to alleviate any possible variation at the edge of the footprint due to attitude control variations. It will therefore be tentatively assumed that only the swath width illuminated at periaapsis will be processed throughout the mapping strip and that the processed swath will lie at the near edge of the swath in order to ensure maximum latitude coverage. This introduces a complexity in that the returns must now be integrated between certain time intervals only. Also, the start of this time interval must change with the spacecraft altitude. Some scheme using an altimeter or the doppler frequency shift from the center of the footprint (or its time integral) as an indicator of the instantaneous altitude must be incorporated in the radar system. This may be necessary in any event for elliptic orbits as there will probably be a need to know the spacecraft's radial velocity at each point in the orbit.

Finally, from a practical standpoint, antenna lengths will be otherwise limited to 15 m in this study.

The required surface resolution also impacts the pulse length, τ , in that the range resolution is limited to $c\tau/2$, where c is the speed of light. The projection of this limitation to the planetary surface produces the requirement that

$$\tau \leq \frac{2\Delta r \cos \psi}{c}$$

where ψ is the angle between the radar beam and the surface (fig. 18(a)). The most stringent condition results from consideration of the edge of the swath nearest the radar, and the pulse length must be designed to accommodate this condition. If pulse compression is used, the effective pulse length resulting from compression must satisfy the above relationship.

Combined Effect

To illustrate the various combined effects of the variables described so far in this section, the swath width has been plotted in figure 22 as a function of orbit eccentricity for a periaapsis altitude of 500 km. Also shown in this same figure are the associated antenna dimensions and the number of

orbits between successive swaths. In all cases the antenna has been sized for a mapping swath between planetary latitudes of $\pm 60^\circ$.

From the previous considerations of orbit insertion (fig. 12(a)), the eccentricity range discussed there (0.2-0.5) can be seen to intersect the one-, two-, and three-revolution curves at $W \approx 50$ km and $L \approx 7$ m. Also, it can be seen in this figure that the antenna can become too long for swath widths of 100 km and too high for swath widths less than 50 km. The antenna height shown is that necessary to exactly illuminate the given swath width at periapsis. If the antenna is limited to 2 m in height, then, for swaths less than 50 km wide, the size of the footprint illuminated will be excessive. This will result in higher transmitter power than would ordinarily be required with a resulting increase in spacecraft weight. As a consequence, swath widths less than 50 km were not considered in this study. Thus, it is possible to isolate a region in figure 22 between the ranges $0.2 \leq e \leq 0.5$ and $50 \leq W \leq 100$ km as being a preferred domain of operation. Other figures of this type have been generated for other values of maximum planetary latitude at radar cutoff. The dominant effect of changing the cutoff latitude is to change the position of the antenna length curve a very small amount. It should be emphasized, however, that these curves are for a fixed 20 percent overlap between successive swaths at periapsis. Thus, there are many curves of this type that could be generated, depending on the scientific value attached to high overlap. A number of other important factors must also be considered before any additional progress can be made in the selection of the various system design parameters.

Power Requirements

Perhaps the most important additional parameter is the power that must be supplied to the spacecraft in general and to the radar system in particular. A convenient expression for radar peak radiated power (ref. 32) is

$$P = \frac{4\pi k T \lambda^2 B R^4 (S/N) \Delta X \Delta r N}{\eta^2 L^2 D^2 \sigma} \quad (13)$$

where

P	peak power, W
k	Boltzmann's constant, J/°K
T	effective receiver temperature, °K
$\frac{S}{N}$	signal-to-noise ratio
B	bandwidth, cps
R	slant range, m

σ	scattering coefficient (a function of incidence angle)
ΔX	azimuth target element, m
Δr	range target element, m
N	number of pulses integrated
η	antenna efficiency
$\ell(R)$	system losses and atmospheric attenuation

The average power can be written

$$\bar{P} = P (PRF) \tau$$

where

$$\tau = \text{pulse duration, sec}$$

Thus,

$$\bar{P} = \frac{KR^4 \lambda^2}{\Delta X \Delta r t_o L^2 D^2} \quad (14)$$

where

$$K = \frac{4\pi kT(S/N) \ell(R)}{\sigma \eta^2}$$

$$B = 1/\tau$$

$$t_o = N/PRF; \text{ integration time, sec}$$

For a fully focused synthetic aperture radar system,

$$t_o = \frac{\beta \frac{R}{V}}{\frac{\lambda R}{LV}} \approx \frac{\lambda R}{LV} \quad (15)$$

Therefore,

$$\bar{P} = \frac{KR^3 \lambda V}{LD^2 \Delta X \Delta r}$$

Equation (16) now contains most of the variables discussed up to this point with the exception of the factor K , which includes the less certain parameters in this analysis. The values used to evaluate K were

$$\frac{S}{N} = 10$$

$$k = 1.38 \times 10^{-23}, \text{ J/}^\circ\text{K}$$

$$T = 1000^\circ \text{ K}$$

$$\sigma = 10.0133 \cos \psi / (\sin \psi + 0.1 \cos \psi)^3 \quad (\text{ref. 32})$$

$$\psi = \text{angle of incidence to surface}$$

$$\eta = 0.85$$

$$10 \log_{10} \ell(R) = (R/H) 0.6 f^2 + 3 \text{ dB} \quad (\text{ref. 31})^2$$

Actually, many other choices for these parameters could be justified here, but these were selected as typical. Furthermore, there is considerable general uncertainty about T , σ , and the required value of S/N (for a more detailed discussion, see ref. 2). Thus, it would not appear that greater detail could be justified for a preliminary analysis of this sort; rather a search will be made for regions of interest using a typical value of K before going into more detail.

Again, there is a large number of interacting variables and requirements. From the discussion of the science requirements, a value of 100 m appears to be the maximum acceptable value for both Δr and Δx . The selection of frequency is more complicated as it affects antenna size and power as well as the science information. From equations (6), (7), and (11) come expressions for antenna length and vertical height which can be substituted into equation (16):

$$\bar{P} = \frac{KHcW \tan \alpha}{12.5\lambda \Delta r \Delta x} \quad (17)$$

This shows that a long wavelength is desirable from a power standpoint. However, at longer wavelengths, the antenna will need to be very large to keep the desired surface swath at periapsis. From a practical standpoint, construction of very large antennas for space operation is a dominant problem; thus the lowest wavelength consistent with atmospheric attenuation limits is often used. A wavelength of 13 cm appears to be adequate from this point of view and is selected for use here.

The power computed by equation (17) is just the emitted radar power and not the input (dc) power to the radar system. From the analysis of Klopp

²The 3 dB has been added to account for system losses.

et al., an estimate of total radar system power is

$$\text{Input power} = 100 + 3\overline{P} \quad W \quad (18)$$

This relation is based on a number of different coherent radar systems and excludes the recorder power.

The total (dc) power levels associated with the region of interest at a range and azimuth resolution of 100 m each are shown in figure 23(a). The same boundaries apply here as before in figure 22 with the limits established on both swath width and eccentricity. In this diagram the points of insertion of the N curves and the eccentricity curves are representative ones that will be investigated later in greater detail. Again, the power is determined at the 60° latitude point.

The 60° latitude limit assumed in figure 23(a) satisfies the minimum requirements for surface coverage described earlier in the science requirements section. Figures 23(b), (c), and (d) show the same relationships for maximum latitudes of 65° , 70° , and 75° . These curves show that the higher eccentricity cases are eliminated as the coverage requirements increase. This results from the fact that the high eccentricity orbits do not reach high latitudes before planet limb runoff occurs; thus the coverage requirements are not satisfied. In general, power levels between 120 and 2000 W (dc) appear necessary for the range of coverages shown. These values are selected by restricting consideration to swath widths between 50 and 100 km (antenna length and height limits).

For any given coverage requirement, percent overlap, and resolution, there will exist a series of spacecraft design possibilities. Those orbits with low eccentricity will correspond to large retro propulsion system mass requirements and to a low spacecraft mass due to the lower power requirement. This situation will be reversed for high eccentricity orbits. Finally, total spacecraft mass (including propulsion) will increase with an increase in the coverage requirement due to the elevated power requirements and the unavailability of highly eccentric orbits that satisfy the higher coverage goals. It should be noted, however, that the planet surface area covered varies as the sine of the maximum latitude so that there is very little change in the area covered by $\Lambda = 60^\circ$ as compared to $\Lambda = 75^\circ$. This will become more important later when the spacecraft designs are considered in more detail.

ORBITAL OPERATIONS

Another factor that must be taken into consideration is the operations the spacecraft must perform during a typical mapping cycle. For circular orbits, continuous mapping is possible but leads to considerable overlap from swath to swath due to the slow rotation of the planet. There can also exist a considerable occultation problem for communication and/or power supply systems. This is illustrated in figure 24, where the orbit period and minimum

unocculted time (complete occultation at apoapsis) are shown as a function of orbit eccentricity for $H_p = 500$ km. This shows that the problem of excessive occultation time is mainly restricted to low eccentricity orbits where about half the orbit period can be spent either in Sun or Earth occultation. In more elliptical orbits, the spacecraft is unocculted most of the time. It is rather clear from this figure that there are two distinct regions in which substantially different spacecraft could operate. First there is the low eccentricity region between $e = 0.0$ and $e = 0.2$ where considerable occultation of the Sun and/or Earth could occur. This region is also characterized by many rotations between mapping swaths unless very high overlap is required. However, it should also be noted that both sides of the planet could be mapped during each orbit, thus reducing the mapping time to 120 days for the whole planet. The higher eccentricity region will generally require the full 240-day rotational period of Venus for complete mapping. However, far fewer orbits are required per mapping swath (see fig. 23) with the time near apoapsis available for communicating data to Earth.

Power Profiles

Considering the previous range of orbit eccentricities indicated by propulsive requirements, the two extreme cases of $e = 0.2$ and $e = 0.5$ will be examined in sufficient detail to identify some of the major power requirements. In particular, the coverage and resolution required determine the data load that must be transmitted during the remaining unocculted time in the orbit. In what follows, the maximum occultation time will be assumed for each orbit to ensure a conservative result that is independent of the particular launch opportunity.

The case of $e = 0.2$ is illustrated in figure 25. From previous figures it can be determined that $N \leq 3$ is required for a swath overlap of ≥ 20 percent. In the case depicted, the swath covers 60° north and south of the equator; mapping will require about 0.5 hour of orbit time every three orbits. If solar cells are used, then the spacecraft will have to be supported by batteries for 0.75 hour per orbit. If the spacecraft orientation is totally dedicated to mapping near periapsis, then power for about 2.75 hours will be supplied by batteries, with the remaining 3 hours (per three orbits) left for battery charging and communications to Earth. Thus, there are strong interactions between the power, radar, and communications subsystems on such an orbit.

In order to generate a power profile for the orbit shown in figure 25, a data rate is determined from the formula

$$\text{data rate} = PRF \left(\frac{W}{\Delta r} \right) G \left(\frac{t_{map}}{t_{send}} \right) \left(\frac{L}{2\Delta X} \right) \quad (19)$$

where

G number of binary bits in the image gray scale

t_{map} time allowed for mapping

t_{send} data transmission time allowed

A number of assumptions about the communications subsystem must also be made before the communications power can be determined. Most of these are best delayed until a later section which will be devoted entirely to the subject of the communications problem. For purposes of discussion here, it will be assumed that a 2-m parabolic antenna is used to communicate on the X-band wavelength over an Earth-to-Venus distance of 1.72 AU. Factors affecting the antenna size and wavelength will be discussed later, but the communications distance is recognizable as a worst possible condition that occurs near the end of all typical 240-day mapping missions covered in the data of figure 7.

Given the assumptions just made about the communications system, solar cell power profiles can be developed, and one is displayed in figure 26 for $e = 0.2$ and $N = 3$. The horizontal axis is the total time for three orbits while the vertical axis is the power required. Powers less than zero are used here to indicate battery discharge periods. For the conditions chosen ($\alpha = 60^\circ$, $\Lambda_{max} = 60^\circ$, resolution = 100 m), the radar powers required are rather small (see fig. 23(a)), but the time to communicate the implied data back to Earth is short, leading to high power requirements for communications. It must be recalled that the occultation assumed for this orbit is maximum and at apoapsis.

Changing to a higher eccentricity orbit affects the allocation of time as shown in figure 27 for the case of $e = 0.5$ and $N = 2$. Comparing figures 25 and 27 shows that the mapping time is almost unaffected, while the occultation time is almost doubled. However, the charging (and communicating) time has increased by a factor of 3. Therefore, the power profile shown in figure 28 reaches lower peak powers and possibly has fewer operational problems than the case shown in figure 26.

Occultations

It is clear from these figures that there is a tendency for solar cell systems to be appropriate for high eccentricity orbits. However, cases that have been examined were based on a selection of worst parameter values. For example, none of the desirable opportunities considered in figures 6 encounter apoapsis Sun occultation except the 1986 and 1988 opportunities, which are type II trajectories. In these cases, occultation occurs first at periapsis and begins at planet arrival; occultation later intersects apoapsis but only near the end of the mission. This assumes that all the orbits are polar and have periapsis over the equator. Since the trajectories, in general, overtake Venus from behind, periapsis will tend to be in front of the planet.

This leads to the occurrence of occultation at periapsis during the early part of the mission sequence. Apoapsis occultation will not occur until the planet has made almost 270° of rotation. By this time, 75 percent of the mapping will have been completed.

Orbit Maintenance

An important factor not considered so far is the spacecraft attitude changes required for elliptic orbits. This will be considered in more detail later in this paper, but some general considerations here are in order. First, at very high eccentricity there will be some limited spacecraft ability to maintain an orbit periapsis within the desired limits. This has already been examined to some degree in figure 12(b). Otherwise, gas reaction control and control-moment gyro systems are two obvious options that should be considered for maintaining spacecraft attitude. Finally, the simpler case of the circular orbit, whatever its propulsive implications, will be the least troublesome case to consider as far as orbital operations are concerned.

In the science requirements section of this report, it was remarked that considerable overlap was a helpful feature, perhaps implying fore and aft viewing of the planet's surface. Although these factors should have been considered here, they have not been because of the large number of other, less specialized, problems that were encountered.

SPACECRAFT SIZING

A number of spacecraft design possibilities were investigated, as constrained within the boundaries of figure 22, which prescribe a preferred operational domain. For each design, computer programs were used to generate radar system designs and estimates of spacecraft weight and support requirements using the relationships previously discussed as well as scaling laws that will be described in this section.

Based on the sizing relationships given in reference 2, the weight of the radar is estimated from

$$w_R = 13.7 + 20.9 \log(P\lambda) , \quad \text{kg}$$

where

P peak radar power, kW

λ operating wavelength, cm

The antenna weight is proportional to its area,

$$w_{\text{ant}} = 4.9L \cdot D, \quad \text{kg}$$

with L and D given in meters. This weight is considered to be appropriate for an erectible antenna, which must supply sufficient structural rigidity to support its nonsymmetrical shape. It should be extended only after orbital insertion to avoid excessive "g"-loading.

The communications and data storage system are determined by the data load. With each pulse of the radar, $W/\Delta r$ measurements are obtained; M of these are presumed and digitized for transmission to Earth using G bits per measurement. With a mapping pass of duration t_{map} and a data transmission period t_{trans} , the resulting data rate is

$$DR = \frac{W \cdot PRF \cdot G}{\Delta r} \cdot \frac{t_{\text{map}}}{t_{\text{trans}}} \cdot \frac{1}{M}, \quad \text{bits/sec}$$

This relationship ignores the housekeeping and other encounter science telemetry which is insignificant compared to that resulting from the mapping experiment.

The transmission period is

$$t_{\text{trans}} = N \cdot \text{period} - t_D - t_{\text{map}} - t_{\Delta R}$$

where

M number of returns presumed ($M = 2\Delta X/L$)

N number of orbits per mapping pass

t_D occultation deviation

t_{map} mapping

$t_{\Delta R}$ allowance for orientation of the spacecraft from mapping mode to recharge mode, normal to the Sun, and subsequent return to mapping orientation; assumed to be 0.2 hour

The decision to use only battery power during periapsis was prompted by the fact that the Sun will be occulted at periapsis during some period in the mission. The battery then is designed to maintain the spacecraft and radar during mapping. Data transmission is precluded during this period due to the high radar transmitter power load as well as the difficulty of directing the telemetry antenna at Earth during this phase. Solar occultation throughout the balance of the orbit, the recharge phase, will not be a problem until

close to the end of the mission. Due to the high efficiency of solar panels at Venus, the effect of occultation on spacecraft design is minimal, particularly in moderately eccentric orbits. Therefore, for the baseline approach, solar occultation at apoapsis was included.

For spacecraft power, solar cells offer the lightest and most reliable source. Even with performance degradation due to heating of the cells, which occurs due to the proximity of Venus to the Sun, the increased flux more than compensates for the loss of efficiency. Thus, a specific power of at least 185 W/m^2 and 42.5 W/kg are easily achieved, either by means of roll-out arrays or body-mounted cells. The total spacecraft power requirement is on the order of 500 to 700 W, assuming X-band transmitters for telemetry. Thus, a nominal panel area of 4 m^2 would suffice if oriented normal to the Sun, or $\sim 12 \text{ m}^2$ if not oriented or if body mounted. It was found that RTG's, which at best can deliver about 0.9 W/kg , would be excessively heavy for this application and their use consequently was rejected. For energy storage, it was necessary to use a NiCd battery with specific energy of 5.45 W-hr/kg and depth of discharge of 0.50, due to the large number of operational cycles.

Attitude control could be implemented by means of control moment gyros, due again to the number of orientation cycles.

As indicated above, Earth occultation is of concern only when it occurs outside the mapping period. The communications system was sized assuming the worst case of occultation during apoapsis for each orbit and maximum communications distance.

Calculations were performed for each design as previously discussed using a 64 level gray scale ($G = 6$) and a surface resolution of 100 m. As a result, data rates on the order of 70 Kbps and storage of about 10^9 bits was demonstrated to be a common requirement for all cases of interest. Both of these requirements are within present capability. Such data rates would require the installation of X-band equipment at the 64-m DSN sites, while the storage requirement can be satisfied by the recorder developed for ERTS, or by a film system.

Table 1 compares the performance of spacecraft-to-Earth data links using S- and X-band frequencies. This comparison assumes a 2-m dish on the spacecraft and the typical case of a 70 Kbps data rate. This antenna was chosen as the maximum size that could be directed toward Earth with a single rotational degree of freedom, while the spacecraft is directed approximately normal to the Sun for activation of the solar panels. The communications distance will always be less than 1.74 AU. A 64-m receiving antenna is assumed at the DSN site. In the time frame of this mission, DSN coverage will be continuous using 64-m antennas. Therefore, site viewing windows need not be considered. The energy ratio of 5 dB is appropriate for high data rates using convolutional encoding with Viterbi decoding for a 10^{-5} bit error rate. The X-band link requires approximately 1/7 of the S-band transmitter power and this facilitates the entire spacecraft design. As a consequence, an X-band link is preferred for this application. Alternatives do exist, however; specifically, the solar panel may be articulated to point toward the Sun while the spacecraft

body is directed toward Earth and the radar antenna used for communications. Due to the high gain of the radar antenna this would tend to reduce the transmitter size and so permit more extensive consideration of an S-band link. A more thorough study of alternatives is necessary to ascertain an optimum configuration.

For each spacecraft design and its corresponding data rate, the effective radiated power at X-band is given by

$$ERP = \text{data rate (dB)} + 5.4 \text{ dB}$$

or, for a 2-m dish at X-band, the transmitter radiated power is

$$ERP = \text{data rate (dB)} - 37 \text{ dB}$$

as is shown in table 1. This relationship was used to estimate the transmitter size for each design.

For data storage, two systems must be evaluated for their relative potential. A video tape recorder similar to that developed for ERTS would have the necessary capacity of 10^9 bits and associated data rates. The ERTS recorder is capable of 4000 recording playback cycles, well above the 900-cycle maximum requirement for cases within the boundaries shown in figure 22. The disadvantage of tape recorders is the necessity for erasure of one pass of data in order to record the subsequent pass. One alternative is the use of film recording, often used with side-looking airborne radar (figs. 1-3). It is estimated that the weight and power requirements of a film system adequate to record all the data for this mission would be comparable to a magnetic tape system. In addition, the data may be permanently recorded prior to pre-summing and read out at a later time at higher azimuth resolutions, providing a "zoom capability." The spatial resolution of good films would not be a limiting factor in this process. The number of contrast gray levels is, however, limited by the dynamic range of the film, approximately 100 to 1. Further, film is more sensitive to radiation, although this is not of real concern unless RTG power sources were used. Using magnetic tape, the restricted data rate to Earth and the recorder bandwidth determine the desirable number of levels to which the data is encoded. As a result, further analysis will be necessary to ascertain the preferred system for this application.

For the orbital insertion stage, the following parameters were obtained from reference 34.

$$\text{Inert mass fraction} = 0.14$$

$$I_{sp} = 285 \text{ seconds}$$

The ΔV for periapsis insertion was based on a nominal V_{∞} of 4.44 km/sec and

$$\Delta V = \left(\frac{2\mu}{R_p} + V_\infty^2 \right)^{1/2} - \left[\frac{\mu(1+e)}{R_p} \right]^{1/2}$$

where

R_p periapsis radius

μ gravitational constant for Venus

This value was incremented by 0.75 percent for contingencies and 1.0 percent to approximate gravity losses. This is large enough to include typical allowances for midcourse corrections and orbit trim. No provision was included for rotation of periapsis in this sizing exercise. Using the stated configuration, a computer was used to design a radar and spacecraft including propulsion for each eccentricity and swath width possibility. Total spacecraft weights, including propulsion, are displayed in figure 29. From this figure, it is clear that higher eccentricities and narrow swaths provide the most acceptable weights. Two cases outside the boundary are shown to demonstrate the effect of exceeding the antenna height limitation of 2 m.

Two cases representative of acceptable design were explored in further detail to illuminate subsystem comparisons. Very high eccentricities were not included due to the increasing difficulty of orbit maintenance from solar perturbations and unacceptably large antenna lengths; the exact eccentricity where these become a problem has not been determined here and will require a more detailed examination of spacecraft operations and a more precise specification of the orbit characteristics. Table 2 presents the characteristics and subsystem weights of these designs.

A comparison of these two representative designs demonstrates the advantage of higher eccentricity orbits. This results, again, from the lower ΔV requirement coupled with the advantage of longer communications time and longer battery recharge time. The disadvantage lies in the greater radar antenna length that results from a lowered *PRF*. The solar panels specified are quite modest in size due to the high efficiency near Venus, and orientable panels are assumed. As the orbit eccentricity is increased, the required solar panel area decreases. This permits consideration of non-orientable panels and ultimately to body-mounted cells. Both configurations could be overdesigned to compensate for reduced solar viewing cross-sections. The effect on spacecraft weight would be minimal.

No serious technological problems have been encountered for the specified resolutions. The data storage and transmission requirements have been discussed and appear tractable. Thus, increased azimuth resolutions can be considered without changing the mission feasibility. Figure 30 shows the effect of azimuth resolution on transmitter power. For the 0.5 or 0.2 eccentricity cases, a 100 W transmitter would suffice for an azimuth resolution of approximately 15 m. The data storage requirement would also be increased proportionately.

Referring again to table 2, the spacecraft weight is not highly sensitive to eccentricity and is nominally about 550 kg. This is consistent with spacecraft weights, using solar cells, determined by reference 33 for a Venus radar mapping mission.

CONCLUDING REMARKS

Thus, it would appear that a Venus radar mapping mission within the 1980 time period could be accommodated with the launch vehicle and electronic state-of-the-art which could exist at that time. The use of highly eccentric orbits is an interesting approach to meeting the Venus radar mapping requirements. Preliminary Venus approach weight estimates are low enough in many cases to suggest the launching of two tandem spacecraft with a single Shuttle/Centaur or a single spacecraft on the Tital IIIIE/Centaur launch vehicle. Also, the planned Viking propulsion system could be considered with a minimum of modifications, thus obviating the need for a space-storable propulsion system development for this mission. However, the use of elliptic orbits extends the minimum mission mapping time from 120 to 240 days. It is recognized that this creates a variety of lifetime related technology problems for many subsystems.

Ames Research Center
National Aeronautics and Space Administration
Moffett Field, Calif., 94035, February 23, 1973

REFERENCES

1. Anon.: Venus; Strategy for Exploration. Space Science Board, National Academy of Sciences, Washington, D.C., 1970.
2. Klopp, D. A.; Borrough, H.; Goldman, H.; et al.: Orbital Imagery for Planetary Exploration. NASA CR-(73449-54), IIT Research Inst., Chicago, 1970.
3. Smith, H. P., Jr.: Mapping by Radar - the Procedures and Possibilities of a New and Revolutionary Method of Mapping and Charting. USAF, Randolph Field, Texas, 1948.
4. Rydstrom, H. O.: Geologic Map of an Area in Southeastern Arizona Prepared from Radar Photography. Rept. AAP-13730, Goodyear Aerospace Corp., 1961.
5. Fischer, William: An Application of Radar to Geological Interpretation. Proc. First Symp. on Remote Sensing of the Environment, University of Michigan, Ann Arbor, February 13, 14, 15, 1962, pp. 83-84, 1963.

6. Walters, R. L.: Radar Bibliography for Geoscientists. CRES Rept. 61-30, Center for Research in Engineering Science, Univ. of Kansas, Lawrence, Kansas, 1968. (NASA CR-101707)
7. Moore, Richard K.: Radar Imaging Applications: Past, Present and Future. Propagation Limitations in Remote Sensing. AGARD CP-90-71, 1971. John B. Lomax, ed.
8. Reeves, Robert G.: Structural Geology Interpretations from Radar Imagery. Geological Soc. Am. Bull., vol. 80, no. 11, Nov. 1969, pp. 2159-2164.
9. Viksne, A.; Liston, T. C.; and Sapp, C. D.: SLR Reconnaissance of Panama. Photogrammetric Eng., vol. 36, 1970, pp. 253. (Also in Geophysics, vol. 34, no. 1, Feb. 1969, pp. 54-64.)
10. MacDonald, Harold C.: Geological Evaluation of Radar Imagery for Darien Province. Mod. Geol., vol. 1, no. 1, 1969, p. 63.
11. Wing, Richard S.: Structural Analyses from Radar Imagery, Eastern Panamanian Isthmus. Ph.D. Thesis; Tech. Rept. 133-15, Center for Research in Engineering Science, Univ. of Kansas, Lawrence, Kansas, 1970.
12. Wing, Richard S.: Structural Analysis from Radar Imagery: Eastern Panamanian Isthmus. Mod. Geol., vol. 2, no. 1, 1971, pp. 1-21; and vol. 2, no. 2, 1971, pp. 75-127.
13. Terry, Robert A.: A Geological Reconnaissance of Panama. California Academy of Science Occasional Paper 23 (in ref. 11), Mar. 2, 1956.
14. MacDonald, H. C.; Kirk, J. N.; Dellwig, L. F.; and Lewis, A. J.: The Influence of Radar Look-Direction on the Detection of Selected Geological Features. Proc. Sixth Intern. Symp. Remote Sensing of the Environment. Univ. of Michigan, Ann Arbor, Oct. 13-16, 1969, vol. 1, pp. 637-650.
15. Badgley, P. C.; and Lyon, R. T. P.: Lunar Exploration from Orbital Altitudes. N. Y. Acad. Sci. Ann., vol. 123, 1965, p. 1198.
16. Dellwig, Louis F.: An Evaluation of Multifrequency Radar Imagery of the Pissgah Crater Area, California. Mod. Geol., vol. 1, no. 1, 1969, pp. 65-73.
17. Konashenok, V. N.; and Kondratyev, K. Ya.: New Information on Venus and Mars. NASA TT F-692, 1972.
18. Evans, J. V.; Hagfors, T.; Ingalls, R. P.; et al.: Radar Studies of Venus at 3.8 cm Wavelength. Proc. Conf. on Scientific Applications of Radio and Radar Tracking in the Space Program. Pasadena, Calif., April 9-10, 1969; Jet Propulsion Lab. Tech. Rept. 32-1475, 1970, pp. 127-144.

19. Richter, Kurt R.: Enhanced Microwave Absorption in the Lower Atmosphere of Venus. *Radio Sci.*, vol. 7, no. 4, April 1972, pp. 443-447.
20. Cooper, J. R.: Geologic Evaluation - Radar Imagery of Twin Buttes Area, Arizona Test Site 15. U. S. Geol. Survey Tech. Letter NASA-28, 1966.
21. Dellwig, L. F.; and Moore, R. K.: The Geological Value of Simultaneously Produced Like- and Cross-Polarized Radar Imagery. *J. Geophys. Res.*, vol. 71, July 15, 1966, pp. 3597-3601.
22. Ellormeier, R. D.; Fung, A. K.; and Simonett, D. S.: Some Empirical and Theoretical Interpretations of Multiple Polarization Radar Data. *Proc. Fourth Symp. on Remote Sensing of the Environment*, Univ. of Michigan, Ann Arbor, April 12, 13, 14, 1966, pp. 657-670.
23. Gillerman, E.: Investigation of Cross-Polarized Radar on Volcanic Rocks. CRES-TR-61-25, Center for Research in Engineering Science, Univ. of Kansas, Lawrence, Kansas, 1967 (NASA CR-88081).
24. Schwarz, David E.; and Cospall, Fred: The Use of Radar in the Discrimination of Agricultural Land Use. *Proc. Fifth Symp. on Remote Sensing of the Environment*, Univ. of Michigan, Ann Arbor, April 16, 17, 18, 1968, pp. 233-247.
25. Richmond, G. M.: Geologic Evaluation of Anomalies Between Like-Polarized and Cross-Polarized K-band Side-Looking Radar Imagery of Yellowstone National Park. NASA CR-121419; NASA 165, 1970.
26. Schaber, G. G.: Radar Images - Meteor Crater, Arizona. Tech. Letter NASA-62, U. S. Geological Survey, Flagstaff, Arizona, 1966.
27. Smith, Lewis L.; and Gross, Stanley H.: The Evolution of Water Vapor in the Atmosphere of Venus. *J. Atmosph. Sci.*, vol. 29, no. 1, Jan. 1972, pp. 173-178.
28. Rogers, A. E. E.; and Ingalls, R. P.: Venus: Mapping the Surface Reflectivity by Radar Interferometry. *Sci.*, vol. 165, no. 3895, Aug. 22, 1969, pp. 797-799.
29. Goldstein, R. M.; and Rumsey, H., Jr.: A Radar Snapshot of Venus. *Sci.*, vol. 169, no. 3949, Sept. 4, 1970, pp. 974-977.
30. Campbell, D. B.; Jurgens, R. F.; Dyce, R. B.; Harris, F. S.; and Pettengill, G. H.: Radar Interferometric Observations of Venus at 70-Centimeter Wavelength. *Sci.*, vol. 170, no. 3962, Dec. 4, 1970, pp. 1090-1092.
31. Brown, W. E., Jr.; Elachi, C.; Jordan, R. L.; Laderman, A.; and Thompson, T. W.: Planetary Imaging Radar Study. JPL Document 701-145, June 1, 1972.

32. Greenberg, J. S.: A Systems Look at Satellite-Borne High-Resolution Radar. RCA Rev., vol. XXVIII, no. 4, Dec. 1967, pp. 679-709.
33. Brandenburg, R. K.; and Spadoni, D. J.: Preliminary Analysis of Venus Radar Missions. IIT Research Inst. Rept. M-32, Nov. 1971.
34. Scofield, W. T.: A Study of System Requirements for Phobos/Deimos Missions. NASA CR-112077-2, June 1972.
35. Planetary Flight Handbook, NASA SP-35, Part 2. Supplementary Trajectory Data: Earth to Venus and Earth to Mars, 1963.
36. TRW Systems Group: Study of a Common Solar-Electric Propulsion Upper Stage for High-Energy Unmanned Missions. Final Rept., NASA-CR-114350, vol. 2, July 14, 1971.

TABLE 1.— SPACECRAFT-EARTH DATA LINK COMPARISON FOR A DATA RATE OF 70 Kbps

	S-Band, 2.30 GHz	X-Band, 8.448 GHz
Effective radiated power	51.3 dB	53.9 dB
Transmitter (105 W)	20.2	(14.2 W) 11.5
Antenna gain, 2 m	31.1	42.4
Transmitter and receiver losses	-2.0	-1.5
Pointing loss	-.5	-1.0
Free space loss, 1.74 AU	-268.0	-279.3
Atmospheric attenuation	0	-.2
Receiving antenna, 64 m	61.4	71.5
Total received power	-157.8	-156.6
Carrier channel		
Modulation loss, 1.15 rad	-7.8	-7.8
Received carrier power	-165.6	-164.4
Noise spectral density number	-214.6	-213.4
APC noise bandwidth	10.8	10.8
Received carrier-to-noise ratio	38.2	38.2
Threshold carrier-to-noise ratio	6.0	6.0
Margin	32.2	32.2
Signal channel		
Modulation loss, 1.15 rad	-.8	-.8
Received subcarrier power	-158.6	-157.4
Signal-to-noise ratio	56.0	56.0
Required energy-to-noise ratio	5.0	5.0
Data rate, 1 Mbps	48.5	48.5
Margin	2.5 dB	2.5 dB

TABLE 2.— COMPARISON OF REPRESENTATIVE SPACECRAFT DESIGNS
FOR TWO DIFFERENT ECCENTRICITIES

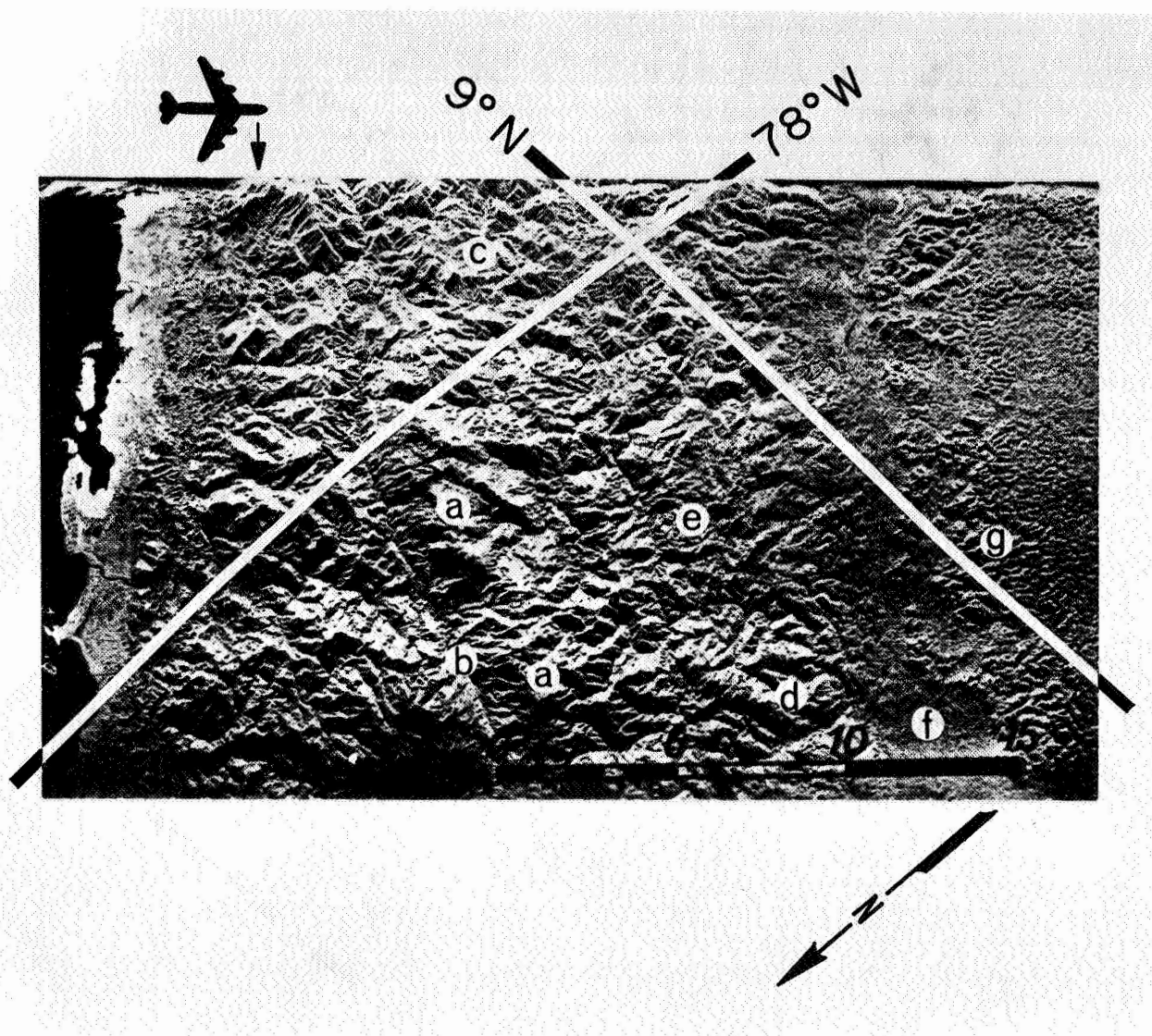
	$e = 0.2$	$e = 0.5$
Orbit		
N	3	2
Swath, km	55.4	74.8
Orbit period, hr	2.27	4.6
Period for N orbits, hr	6.81	9.18
Mapping duration, hr	.53	.52
Solar and Earth occultation,* hr	2.18	2.46
Recharge and communications time,* hr	3.9	6.0
ΔV , km/sec	3.286	2.359
Radar		
Wavelength, cm	13	13
Resolution, km	.1	.1
Pulse length, μ sec	.31	.29
PRF , pps	4983	3615
Antenna length, m	6.2	9.5
Antenna height, m	1.9	1.4
Antenna weight, kg	57	64
Radar average power, W	2.6	17.6
Radar peak power, kW	1.7	17.0
Radar supply power, W	108	153
Radar weight, kg	42	63
Power supply		
Spacecraft power, W	189	185
Recharge power, W	310	221
Telemetry supply, W	53	51
Total demand, W	<u>552</u>	<u>457</u>
Losses and safety factor, W	110	91
Solar Panel requirement, W	<u>662</u>	<u>548</u>
Panel area, m^2	3.6	3.0
Panel weight, kg	15.6	12.9
Power conditioning weight, kg	5.8	5.7
Presun acquisition battery requirement, WH	705	690
Orbital battery requirement, WH	689	710
Total battery weight, kg ($NiCd$)	53.3	53.7

*For N orbits.

TABLE 2.— COMPARISON OF REPRESENTATIVE SPACECRAFT DESIGNS
FOR TWO DIFFERENT ECCENTRICITIES - Concluded

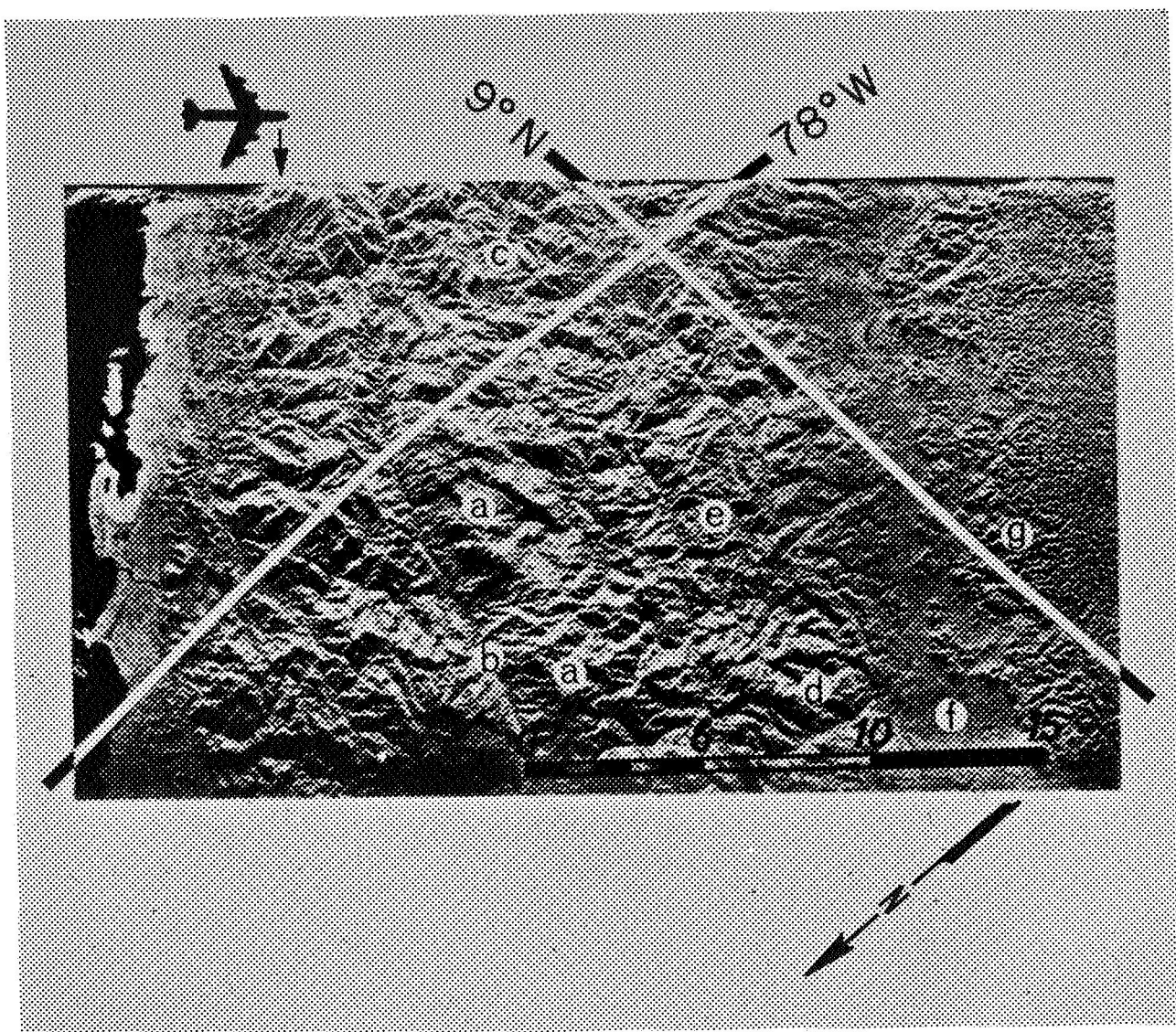
	$e = 0.2$	$e = 0.5$
Communications and data		
Frequency, MHz	8448	8448
Presum number	32	21
Bit rate recorded, Kbps	513	775
Bit rate playback and transmitted, Kbps	70	68
Storage required, bits	0.9×10^9	1.4×10^9
Antenna diameter, m	2	2
ERP required, dB	53.9	53.7
Transmitter RF power, W	14.2	13.6
Transmitter supply power, W	53	52
Spacecraft		
Radar and antenna	98.9	126.8
Data processing	22.7	22.7
Recorder	20.4	20.4
Attitude control	118.6	96.5
Structure and thermal control	135.6	136.6
Cabling	29.3	29.3
Communications	13.1	13.1
Receiver/decoder/sequencer	32.7	31.5
Power supply	74.7	72.3
Spacecraft mass, kg	556.0	549.2
Propellant	1784.6	894.8
Inerts and ullage	249.9	125.3
(Total stage mass)	(2034.5)	(1020.1)
Injected mass, kg	2580.5	1569.3

*For N orbits.



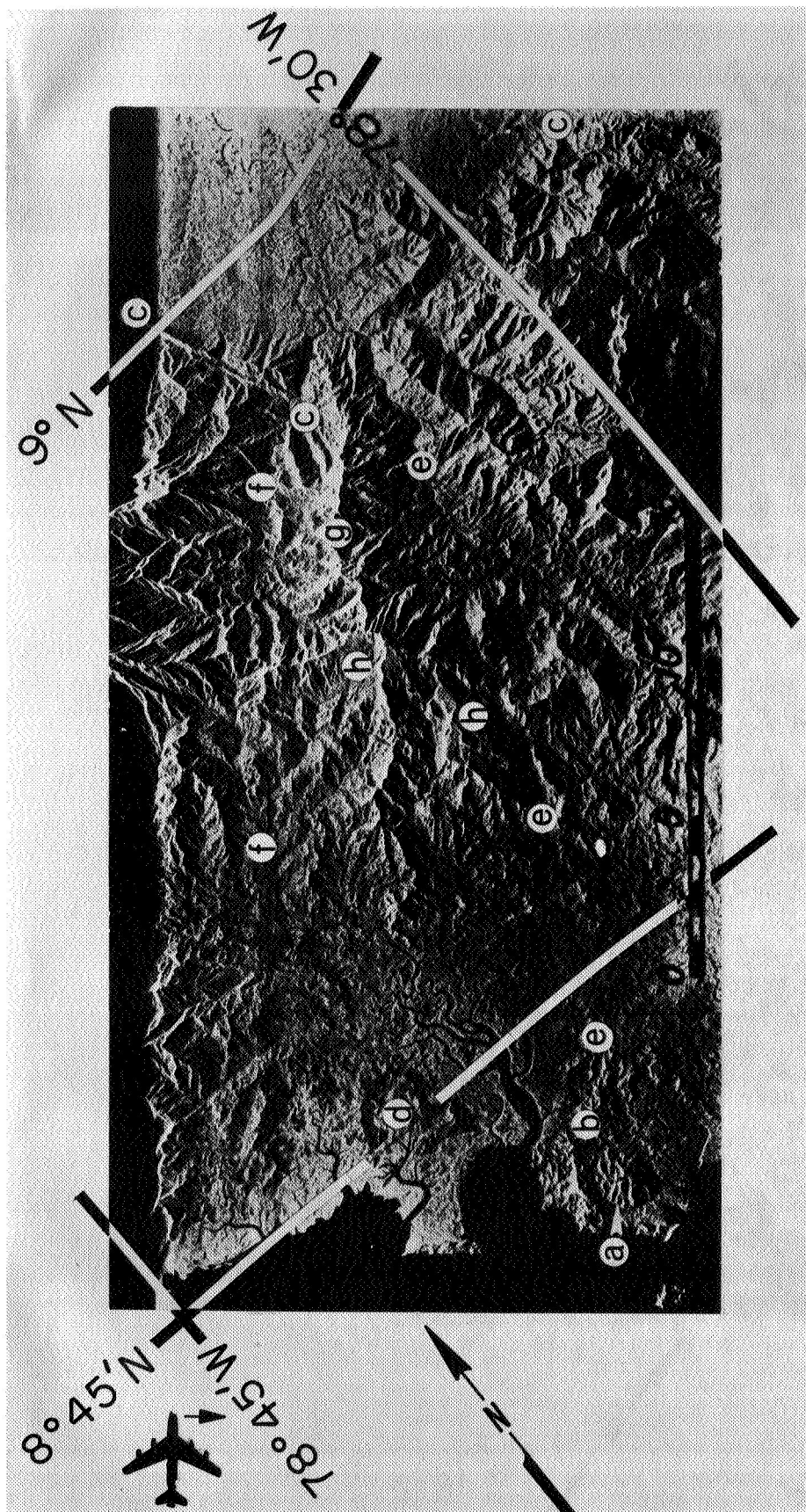
(a) Resolution \approx 15 m.

Figure 1.- Radar imagery of part of the Morti segment of the northwestern Darien Range, showing (primarily) one of the characteristic crestal horst blocks (a) coincident with the Continental Divide and a prominent longitudinal boundary fault (b). A possible ring-dike is at (c). Also displayed are an anticlinal fold (d) and a syncline (e), both expressed in Upper Eocene clastic strata on the south side of the Range. The south-adjacent strike valley (f) manifests the outcrop of southerly dipping Upper Eocene shale. Southerly dipping Lower-Middle Oligocene carbonates (Clarita ls.) are apparent at (g).



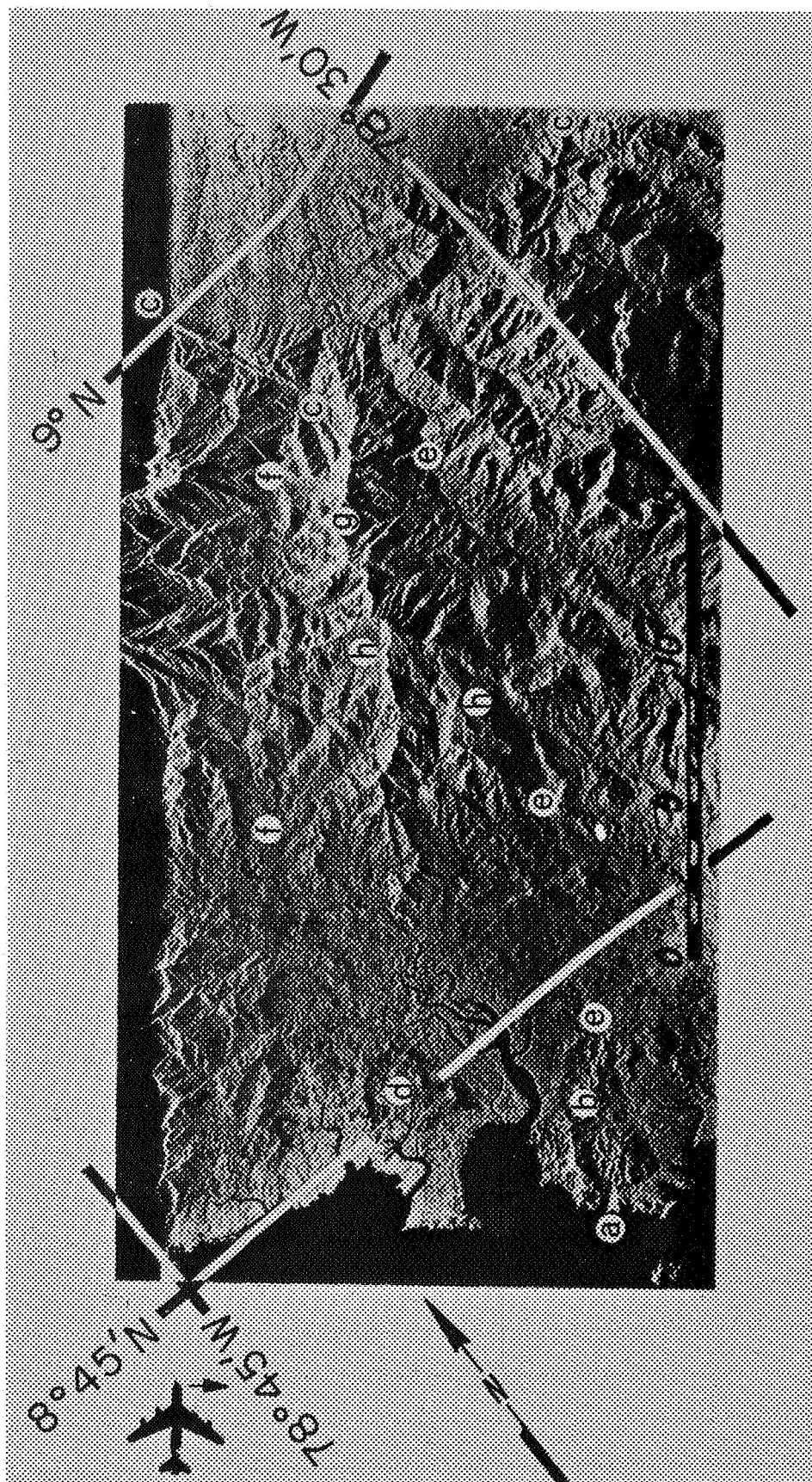
(b) Resolution \approx 100 m.

Figure 1.- Concluded.



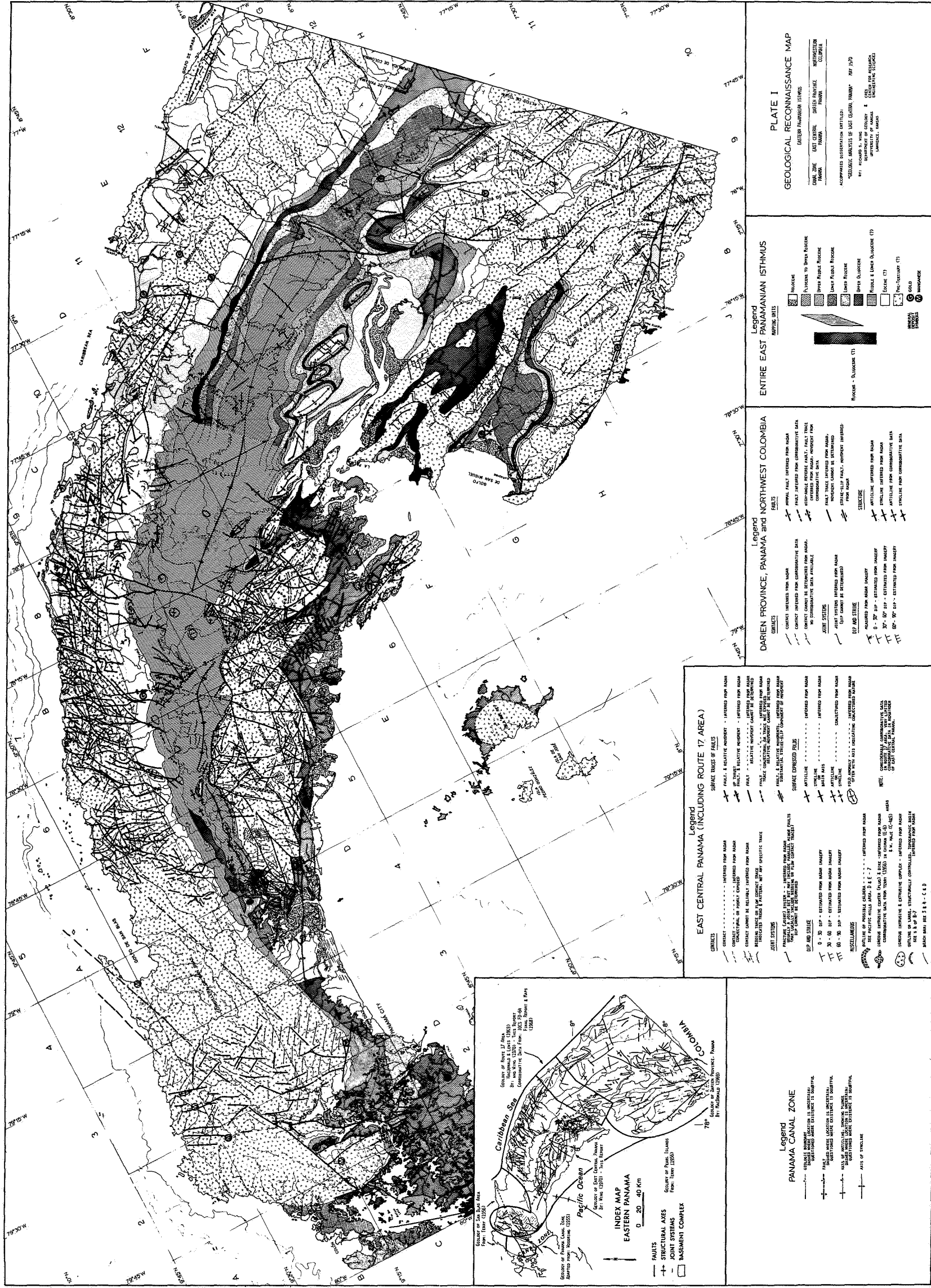
(a) Resolution ≈ 15 m.

Figure 2.- Radar imagery of the Chiman coastal area, adjoining the Gulf of Panama, showing (primarily) the Chiman igneous plug (a) and remnants of its caldera ring (b). Also displayed is a prominent wrench fault (c), another caldera (d), and east-adjacent small plug. This imagery also shows the Chiman fault (e), the West Ipeti fault (f), and the West Ipeti block (g), together with its component Huevito syncline (h). Radar layover and foreshortening in the near range (near the top) are illustrated.



(b) Resolution \approx 100 m.

Figure 2.- Concluded.



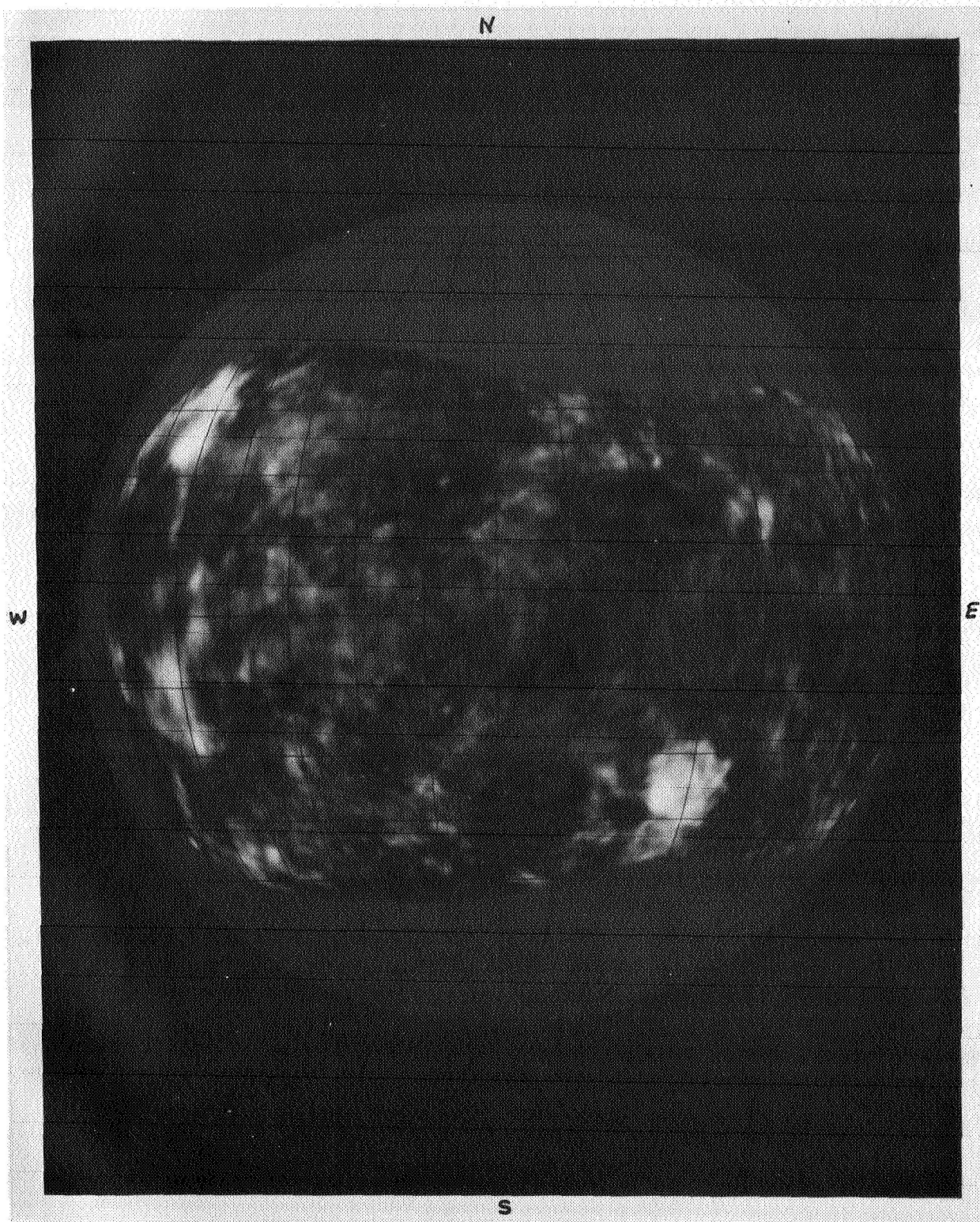


Figure 4.- Goldstone radar map of Venus, June 6, 1972. (Courtesy of Richard Goldstein, JPL)

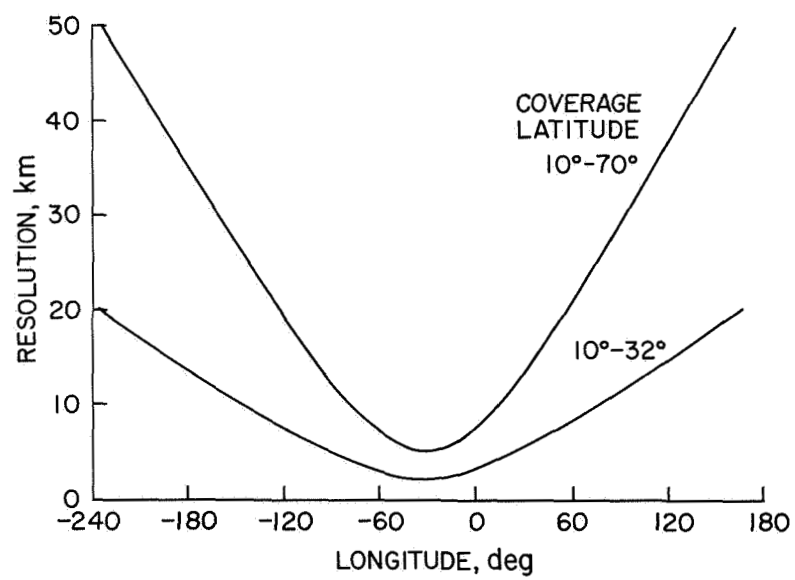
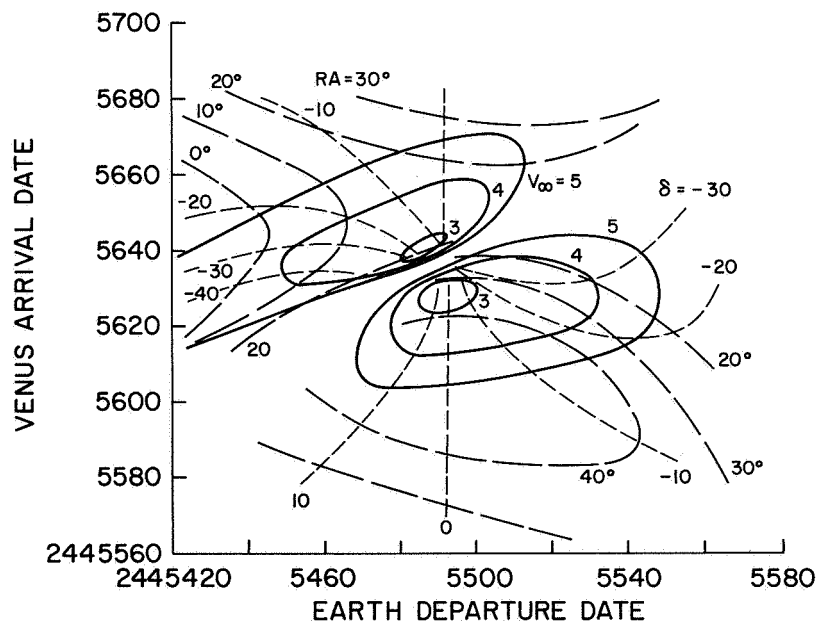
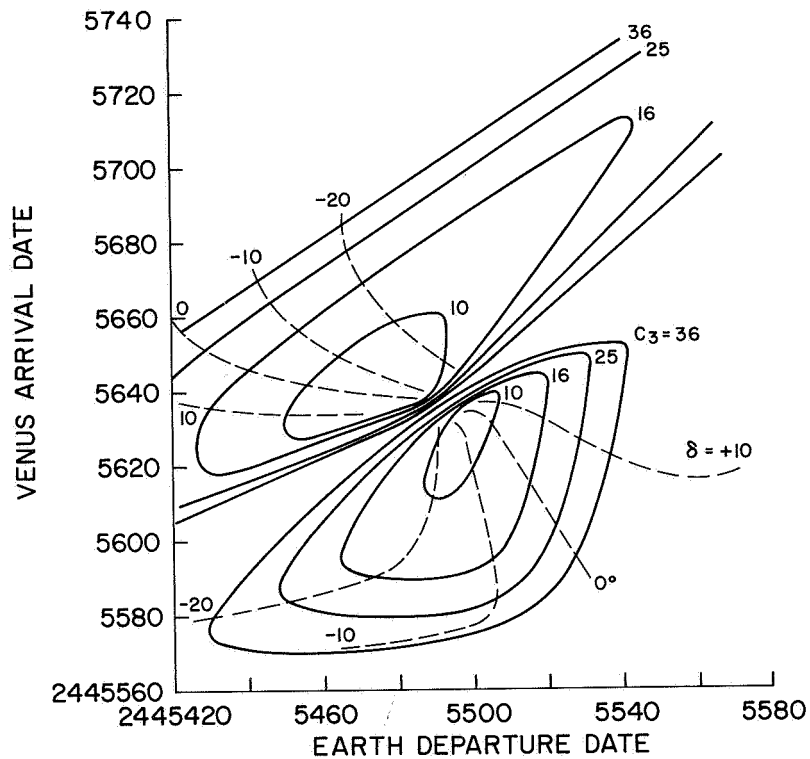
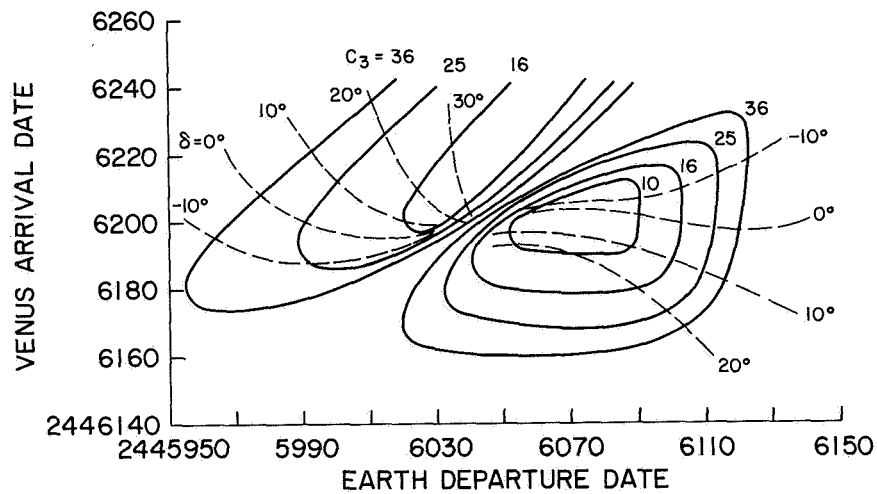
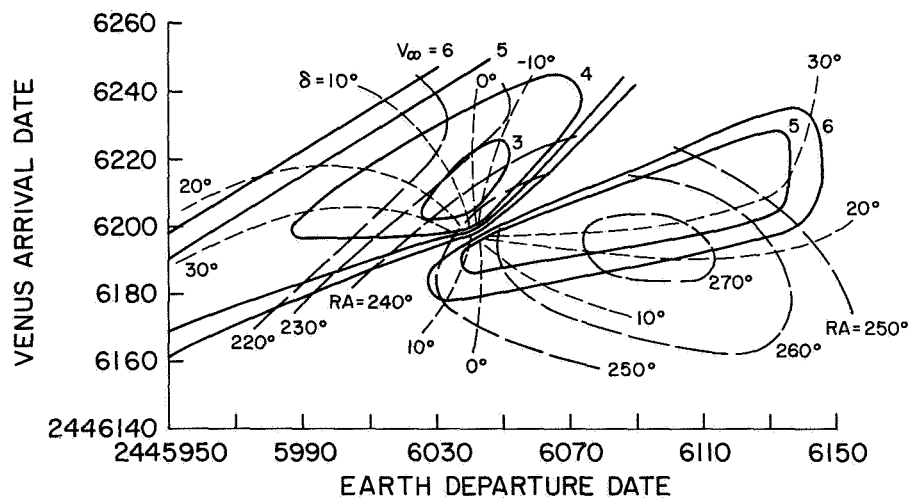


Figure 5.- Future Earth-based capability; Arecibo observational opportunities, 1980, 1988, 1996.



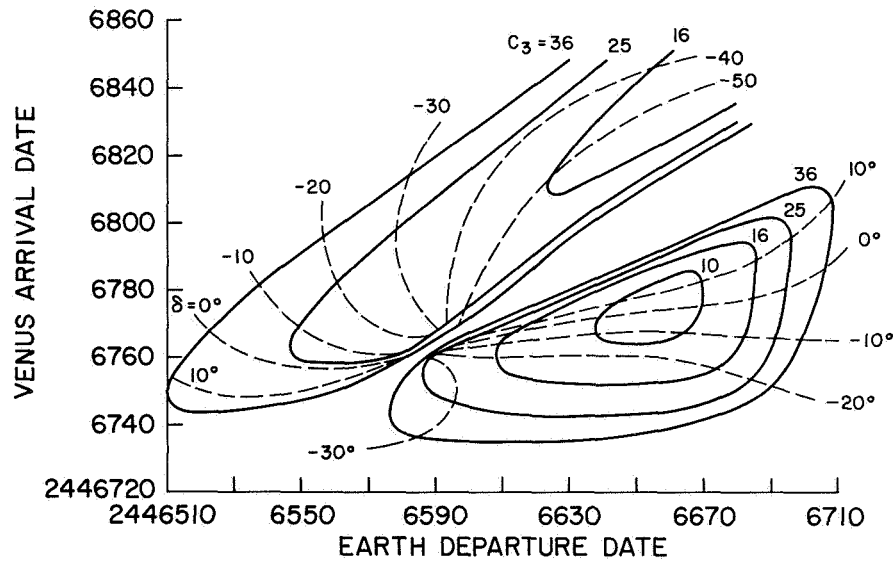


(c) Earth departure characteristics, 1985.

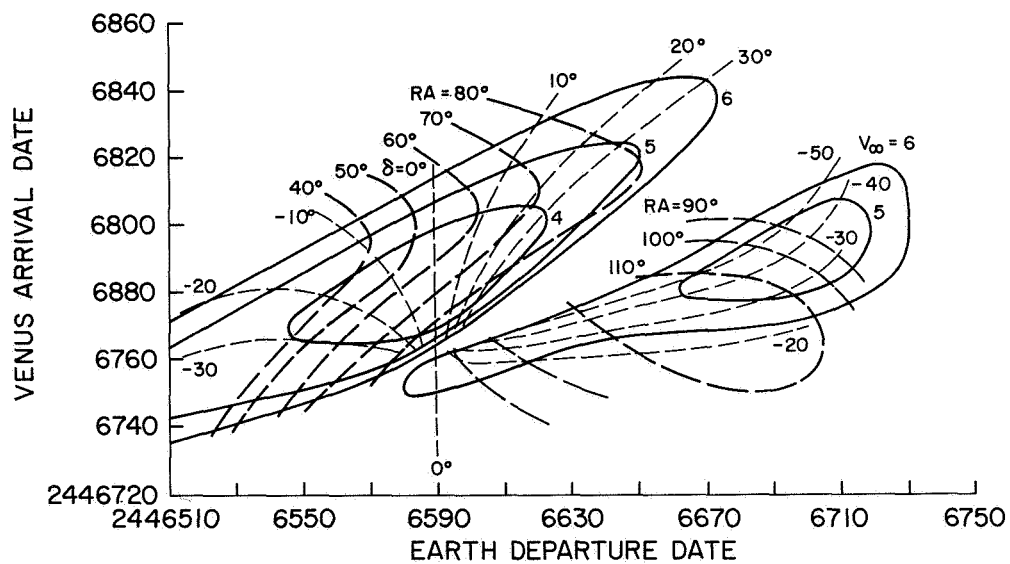


(d) Venus arrival characteristics, 1985.

Figure 6.- Continued.

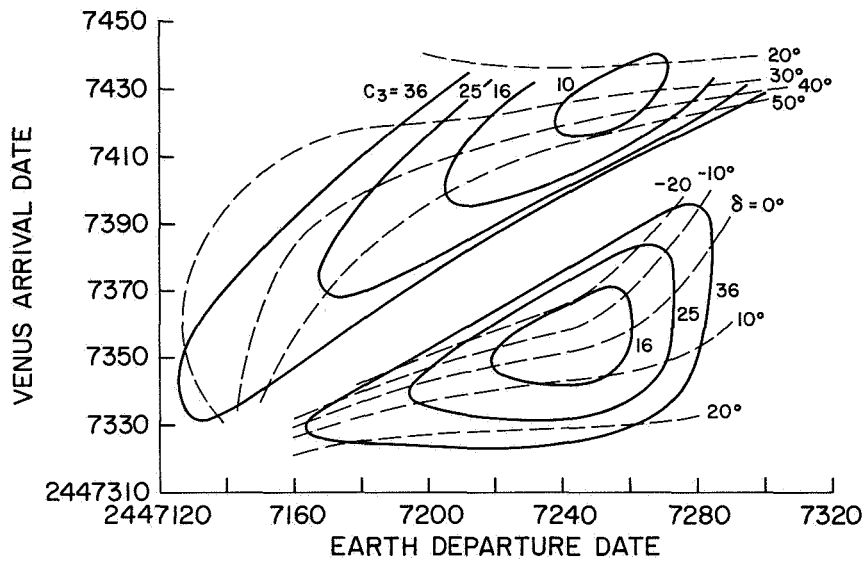


(e) Earth departure characteristics, 1986.

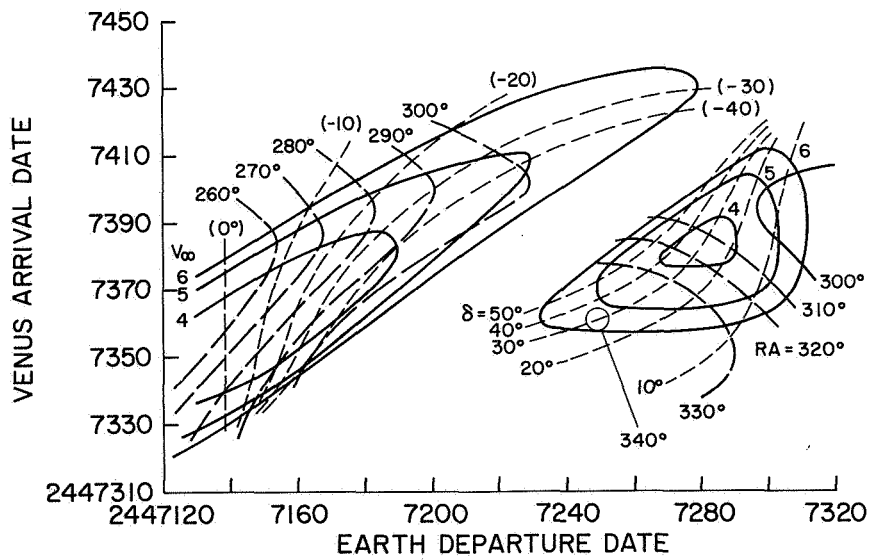


(f) Venus arrival characteristics, 1986.

Figure 6.- Continued.

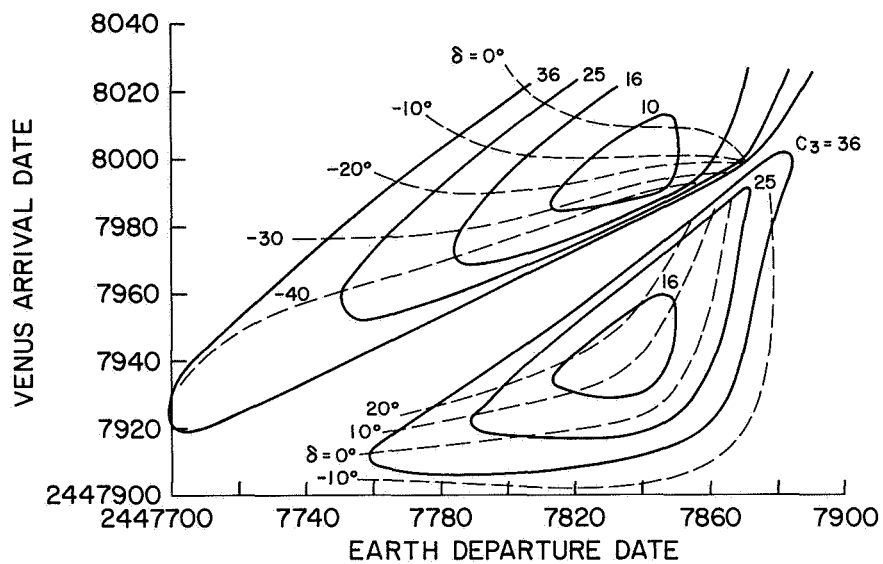


(g) Earth departure characteristics, 1988.

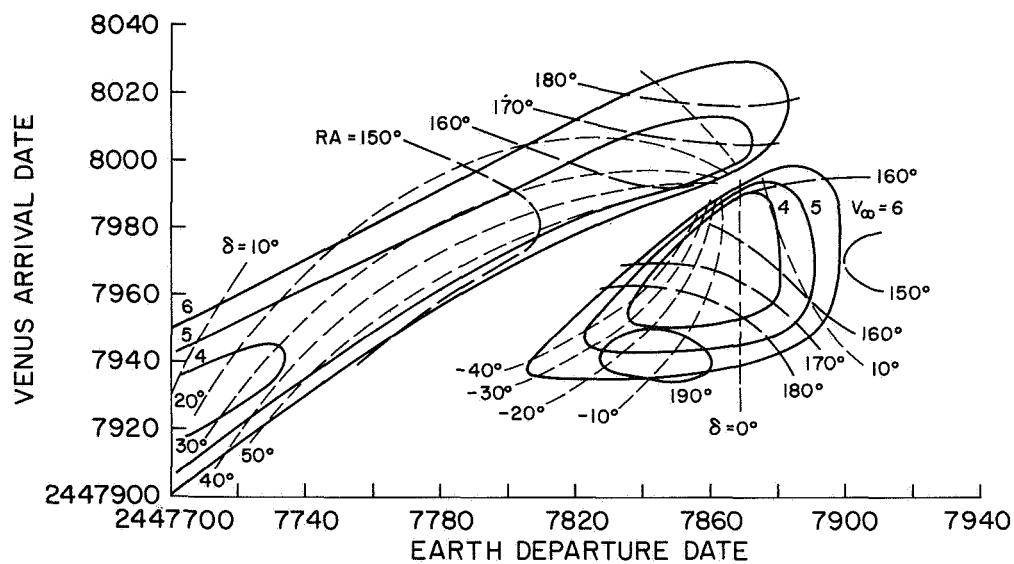


(h) Venus arrival characteristics, 1988.

Figure 6.- Continued.



(i) Earth departure characteristics, 1990.



(j) Venus arrival characteristics, 1990.

Figure 6.- Concluded.

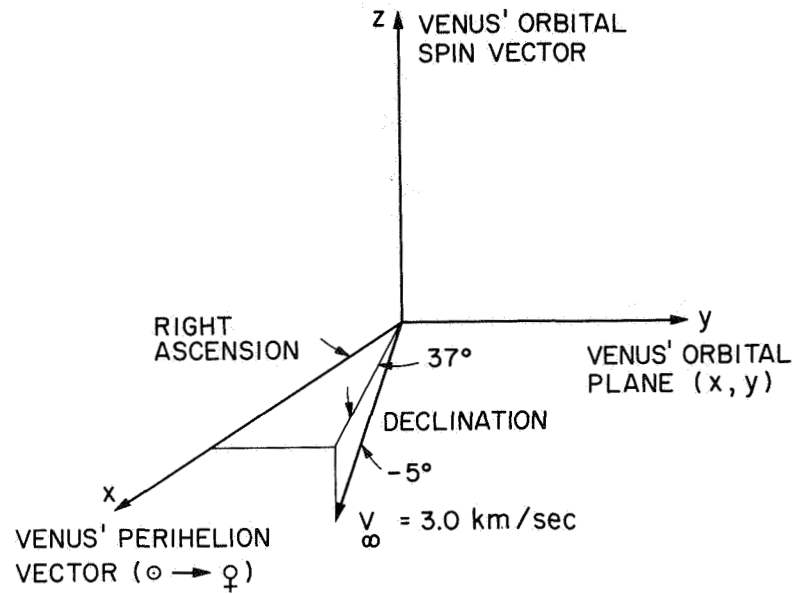


Figure 7.- Coordinate system used for Venus arrival; typical 1983 arrival conditions.

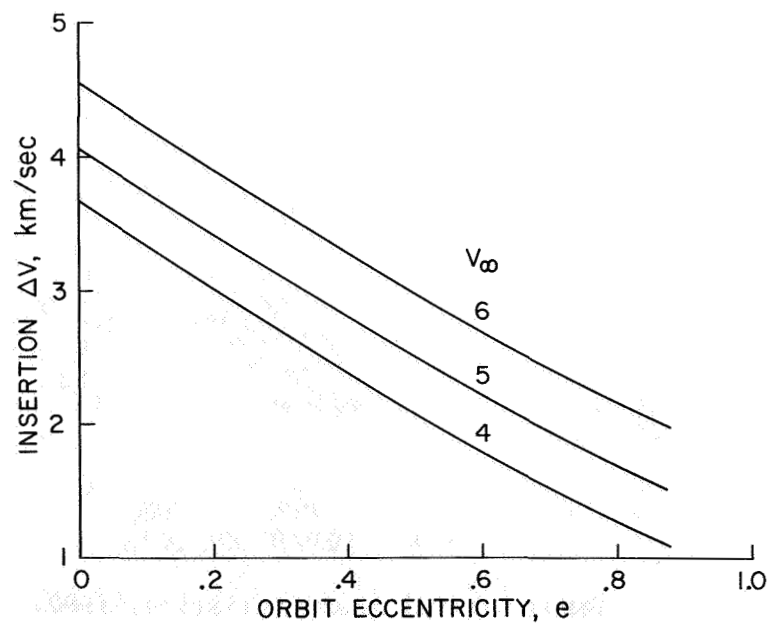
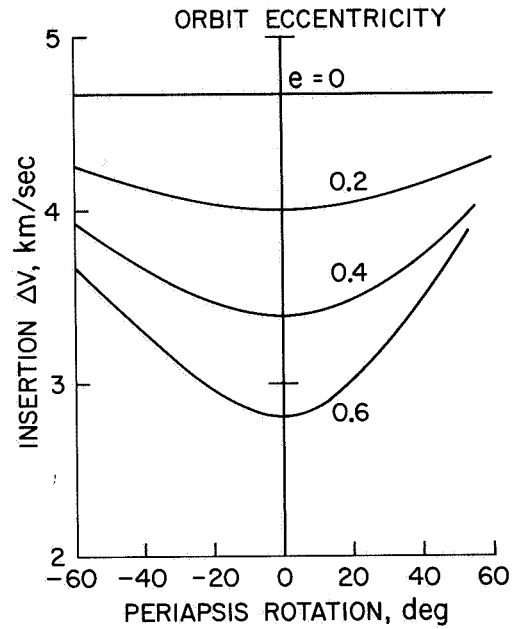
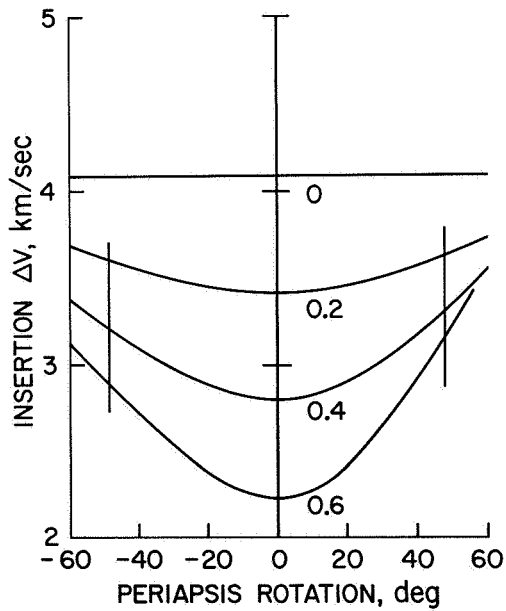


Figure 8.- Velocity requirements for orbit insertion; $H_p = 500 \text{ km}$.

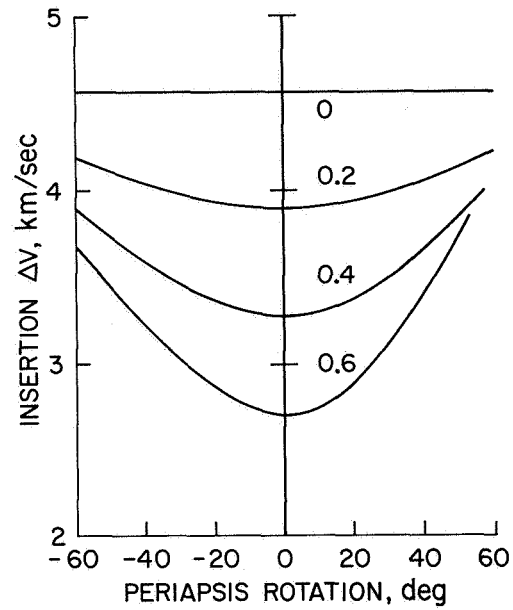


(a) $H_p = 500$ km; $V_\infty = 4$ km/sec, $\epsilon = 40.6^\circ$



(b) $H_p = 500$ km; $V_\infty = 5$ km/sec, $\epsilon = 48.2^\circ$

Figure 9.- Insertion velocity requirements caused by periapsis rotation.



(c) $H_p = 500$ km; $V_\infty = 6$ km/sec, $\epsilon = 54.4^\circ$

Figure 9.- Concluded.

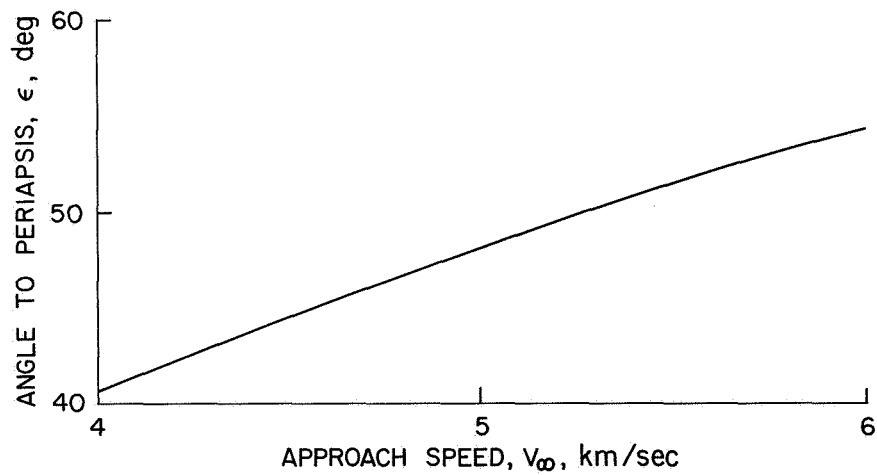
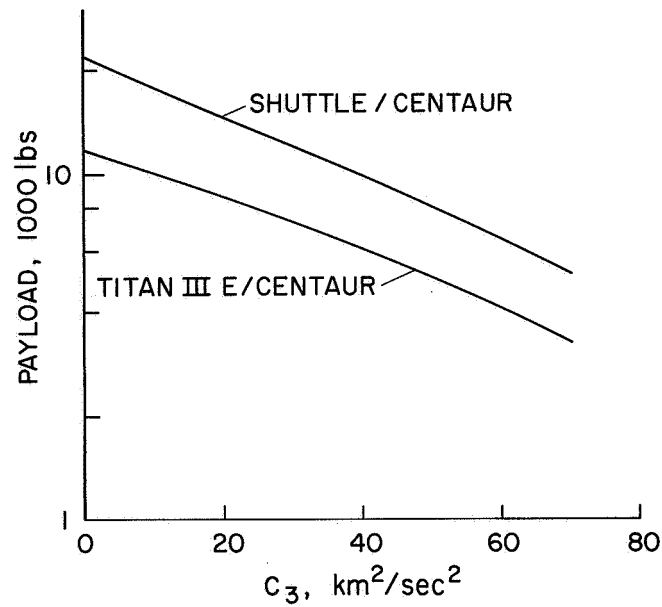
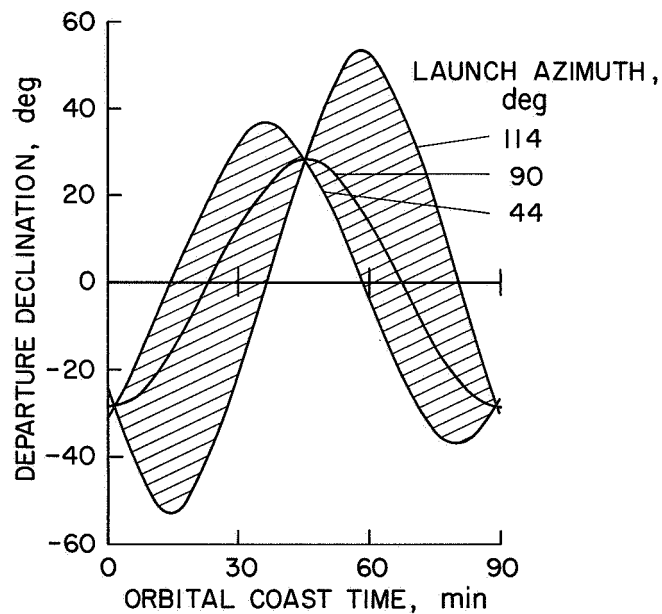


Figure 10.- Position of periapsis relative to approach hyperbola asymptote;
 $H_p = 500$ km.

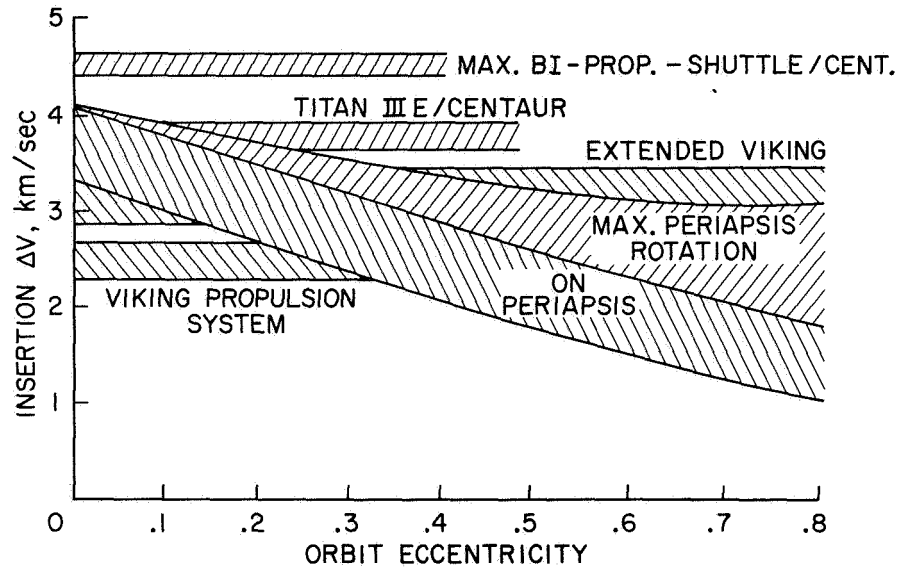


(a) Injected weight at Earth departure.

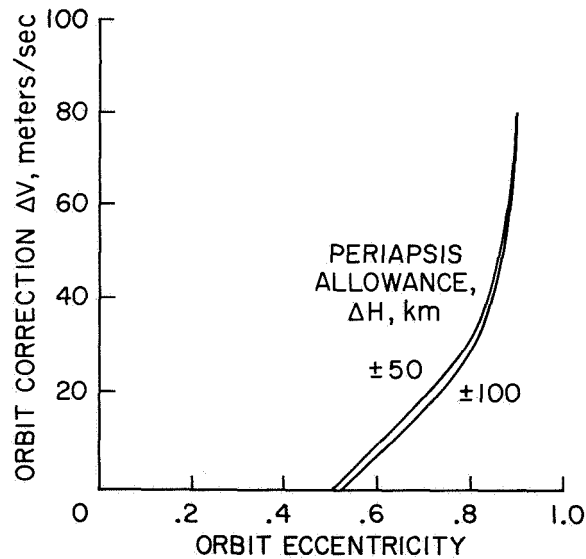


(b) Orbit coast time and departure declination requirements for ETR launch; Titan III E/Centaur launch vehicle, $V_\infty = 0.1 \text{ emos}$ ($C_3 \approx 10 \text{ km}^2/\text{sec}^2$), $H_p = 185 \text{ km}$.

Figure 11.- Launch vehicle capability.



(a) Orbit insertion; $C = 10 \text{ km}^2/\text{sec}^2$, $H_p = 500 \text{ km}$, $V_{HP} = 3.5 \rightarrow 5.5 \text{ km/sec}$.



(b) Orbit maintenance requirements; 1983 opportunity, $H_p = 500 \text{ km}$, $\omega = -26.5^\circ$, $i = 90^\circ$, $\Omega = 37^\circ$, mission time = 240 days.

Figure 12.- Radar orbiter propulsion requirements.

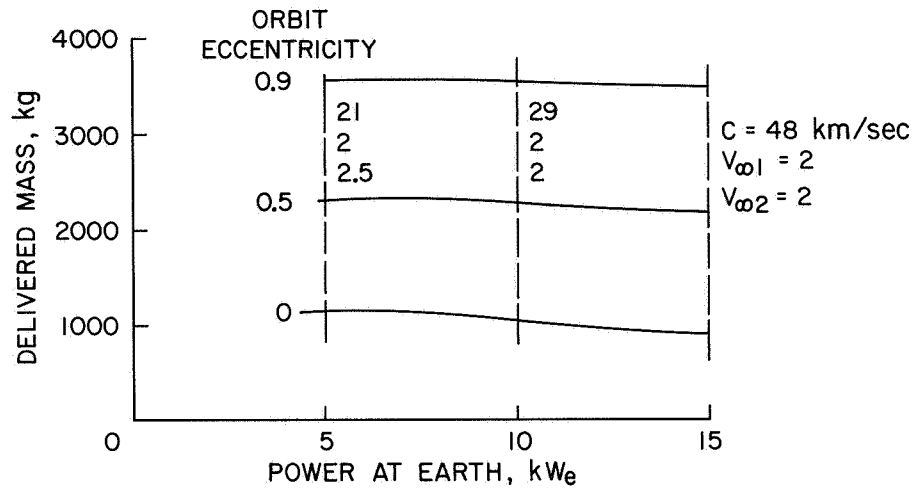


Figure 13.- 1983 SEP Venus orbiter; propulsion system = 30 kg/kWe, flight time = 150 days, $H_p = 1000 \text{ km}$, $I_{sp}(\text{retro}) = 300$, retro tank fraction = 0.10, Titan IIIE/Centaur launch.

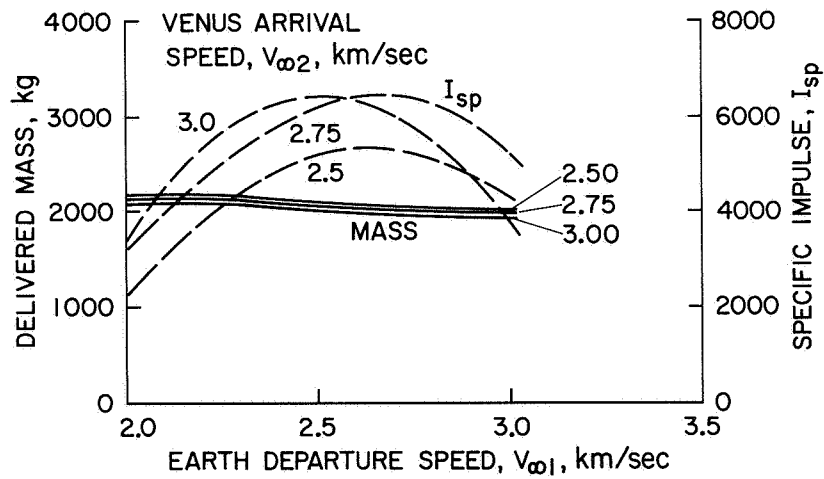


Figure 14.- Characteristics of 1983 Venus orbiter missions; $e = 0.0$, flight time = 150 days, power (at Earth) = 15 kWe, Titan IIIE/Centaur launch.

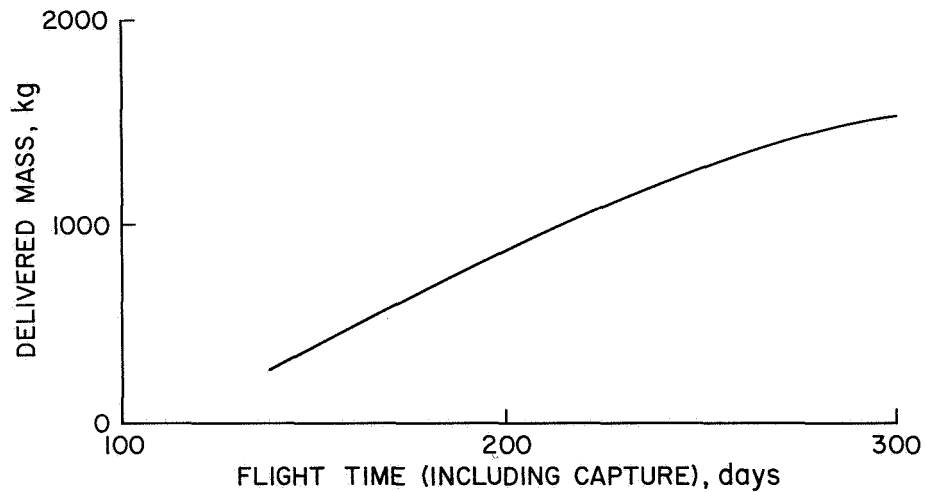


Figure 15.- Low thrust spiral capture for Venus orbiter; power = 15 kWe (at Earth), $e = 0$, $H_p = 1000$ km, Titan IIIIE/Centaur launch, propulsion system = 30 kg/kWe.

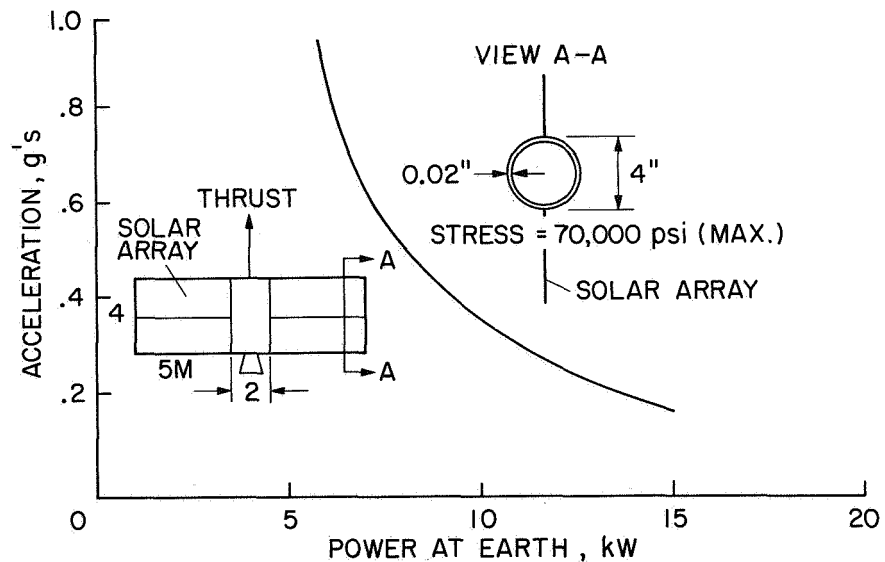


Figure 16.- Solar array acceleration limits; TRW/ACMD design concept.

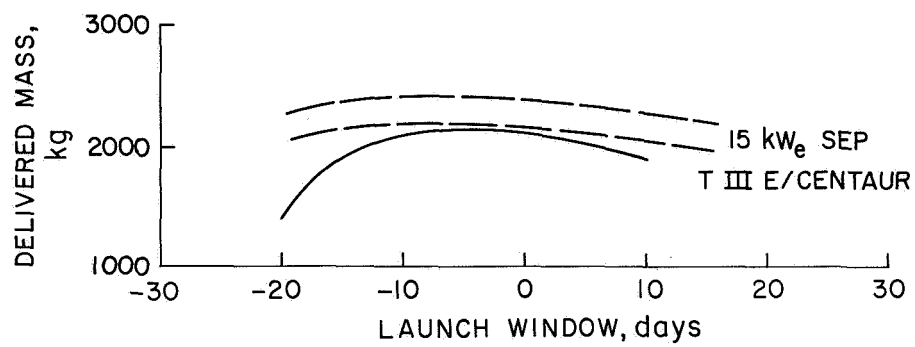
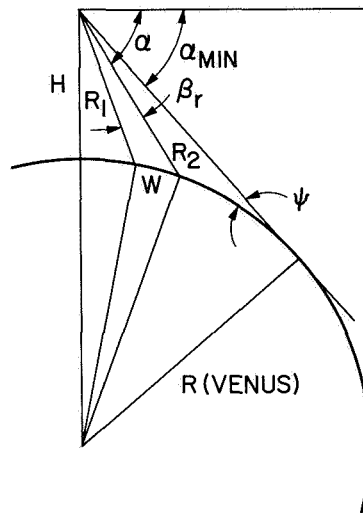
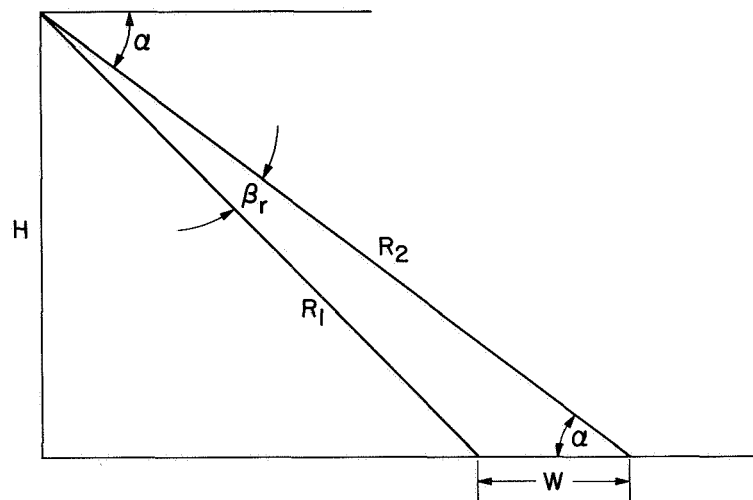


Figure 17.- 1983 Venus orbiter; propulsion system = 30 kg/kWe, $H_p = 1000$ km, $e = 0.5$, flight time = 150 days, $I_{sp}(\text{retro}) = 300$, retro tank fraction = 0.10.



(a) Typical mapping geometry.



(b) Simplified geometry near periapsis.

Figure 18.- Geometric relations for orbital radar mapping.

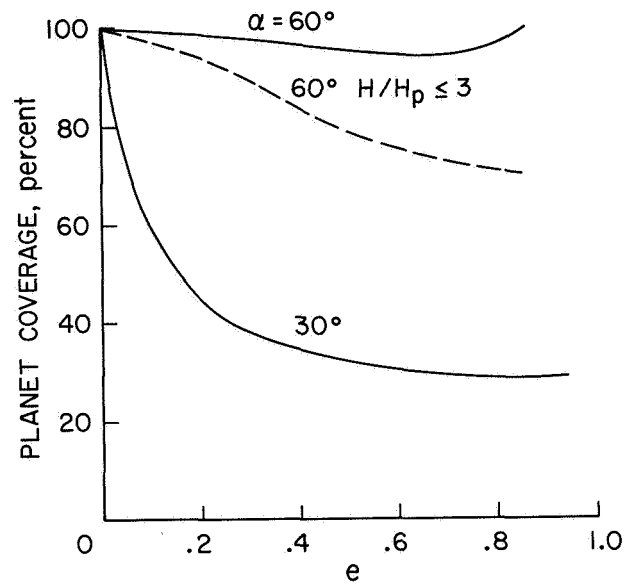


Figure 19.- Relative mapping of planetary surface; $H_p = 500$ km, $N = 1$, 20 percent swath overlap.

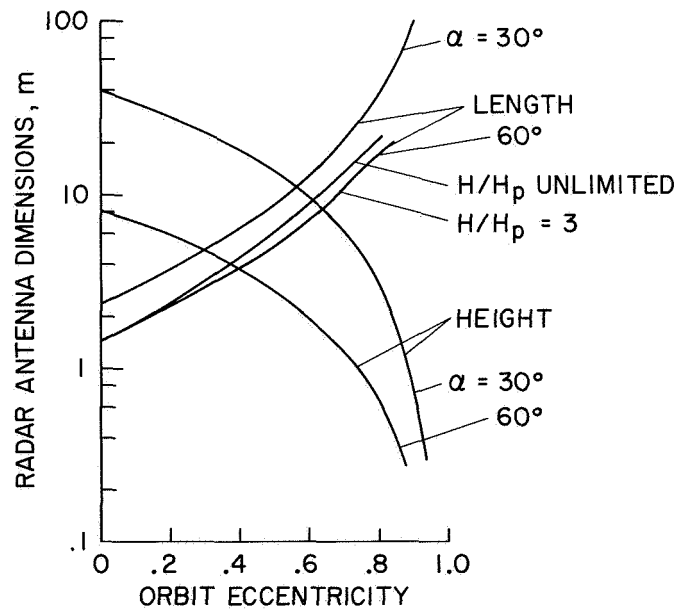


Figure 20.- Radar antenna dimensions vs. eccentricity; $\lambda = 13$ cm, $N = 1$, 20 percent swath overlap, $H_p = 500$ km.

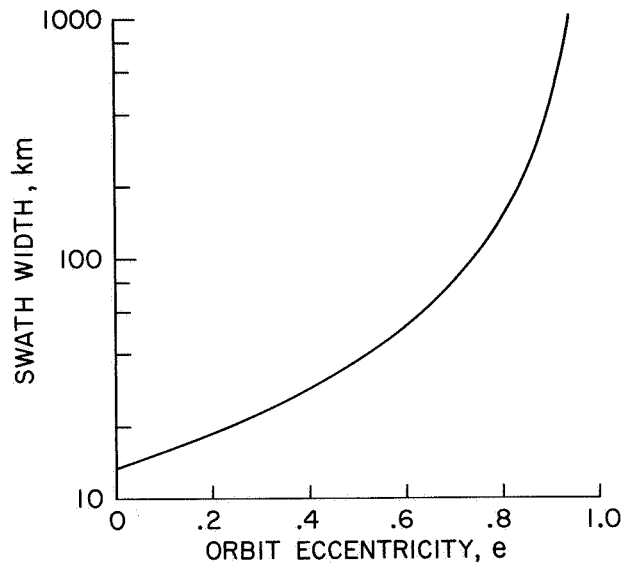


Figure 21.- Swath width at periapsis; $H_p = 500$ km, $H_p = 1000$ km, $N = 1$, 20 percent overlap.

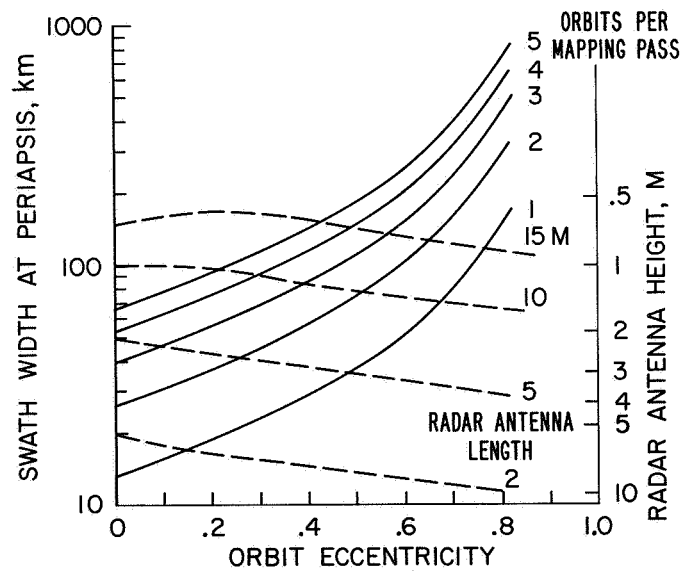
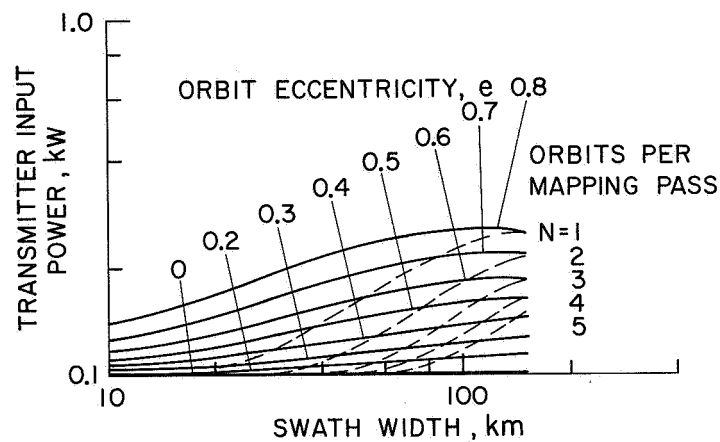
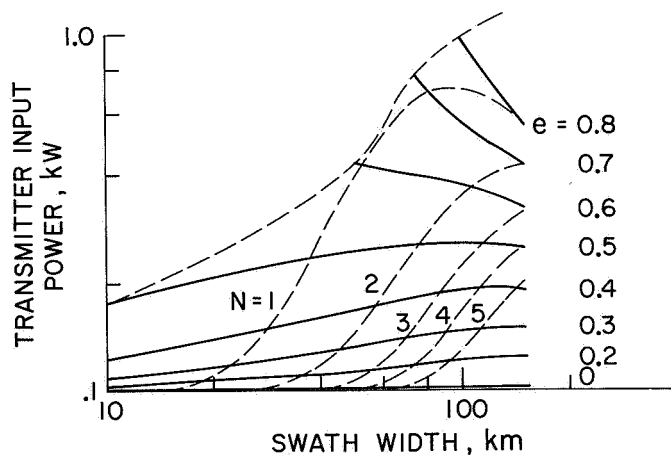


Figure 22.- Radar coverage implications; $H_p = 500$ km, $\alpha = 60^\circ$, $\Lambda_{\max} = 60^\circ$, 20 percent overlap.

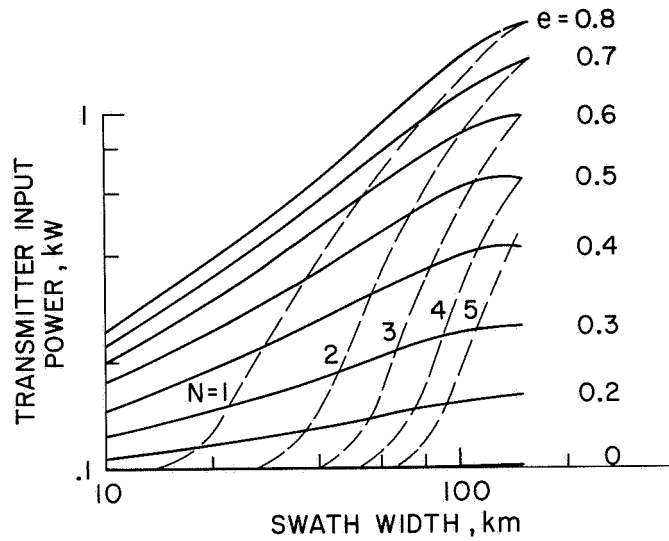


(a) Maximum latitude of coverage, 60°.



(b) Maximum latitude of coverage, 70°.

Figure 23.- Radar power requirements; $H_p = 500$ km, $\lambda = 13$ cm, resolution = 100 m, $\alpha = 60^\circ$.



(c) Latitude of coverage is maximum.

Figure 23.- Concluded.

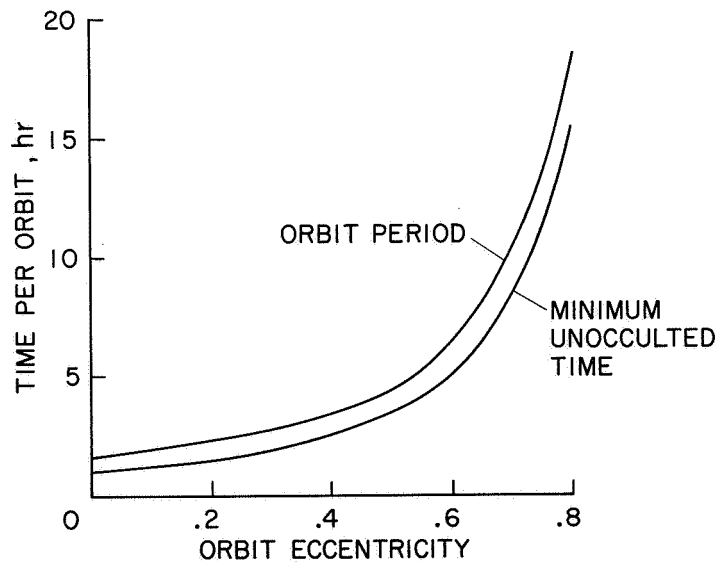


Figure 24.- Occultation time; $H_p = 500$ km.

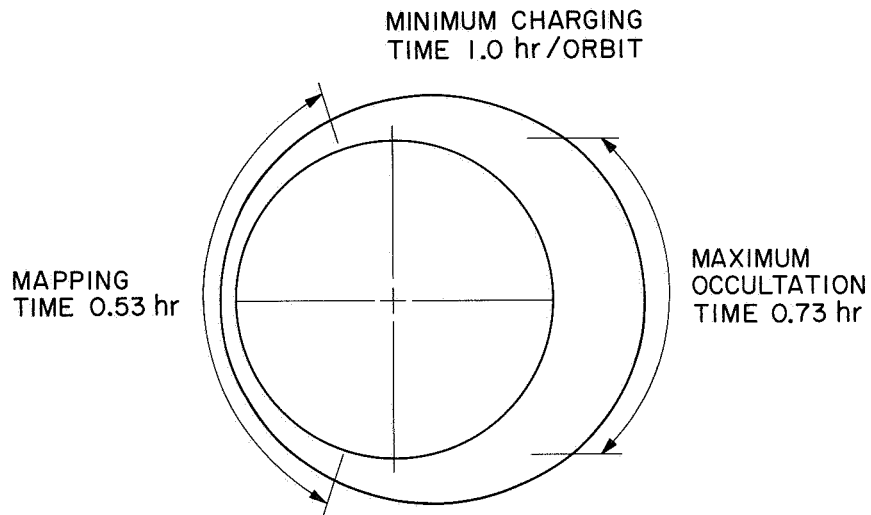


Figure 25.- Mission profile; $e = 0.2$, $N = 3$.

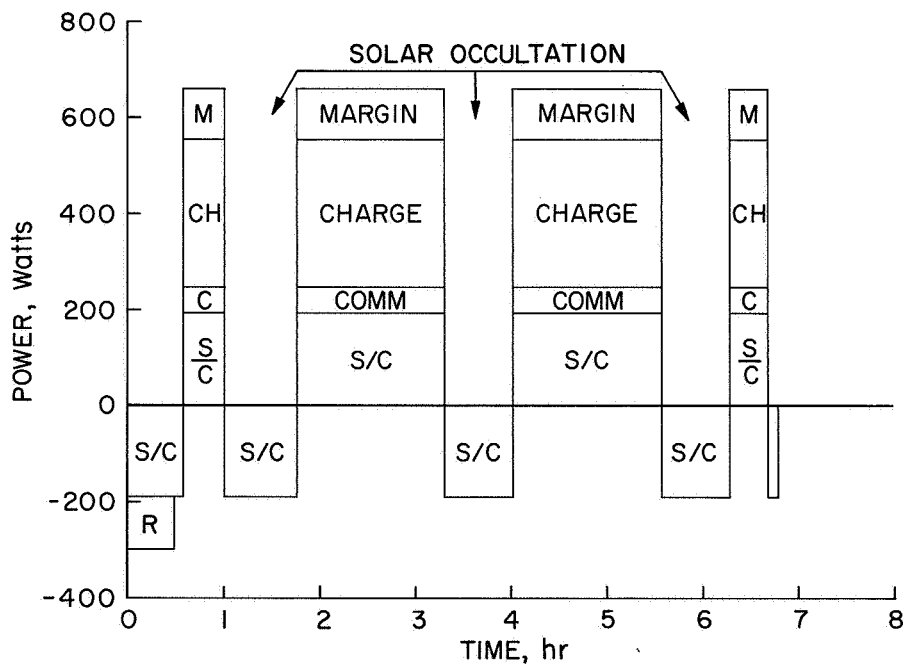


Figure 26.- Spacecraft power profile; $H_p = 500$ km, $\alpha = 60^\circ$,
eccentricity = 0.2, resolution = 100 m, $\Lambda_{\max} = 60^\circ$, $N = 3$,
solar cell power.

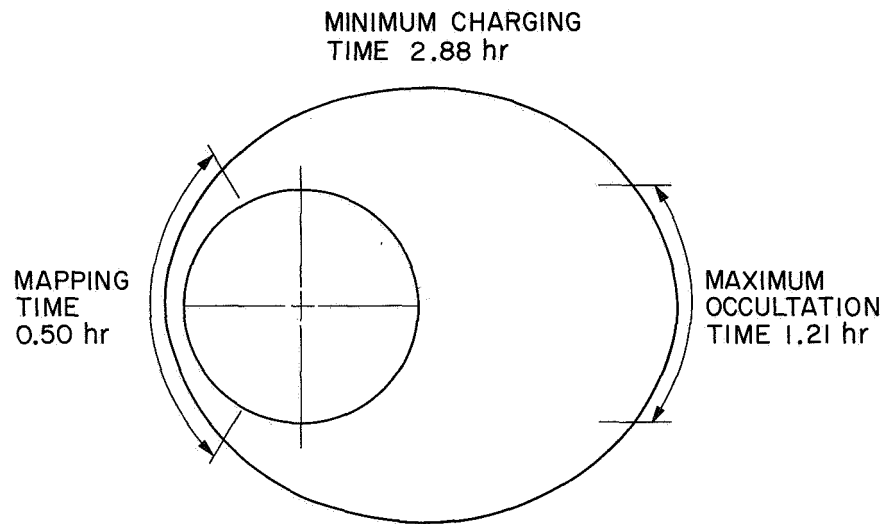


Figure 27.- Mission profile; $e = 0.5$, $N = 2$.

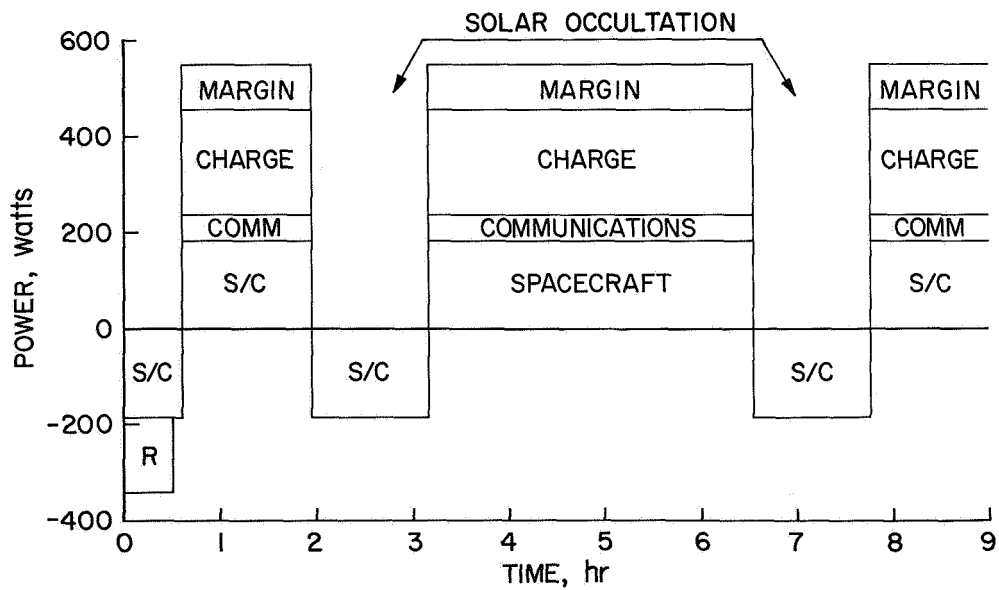


Figure 28.- Spacecraft power profile; $H_p = 500$ km, $\alpha = 60^\circ$, eccentricity = 0.5, resolution = 100 m, $\Lambda_{\max} = 60^\circ$, $N = 2$.

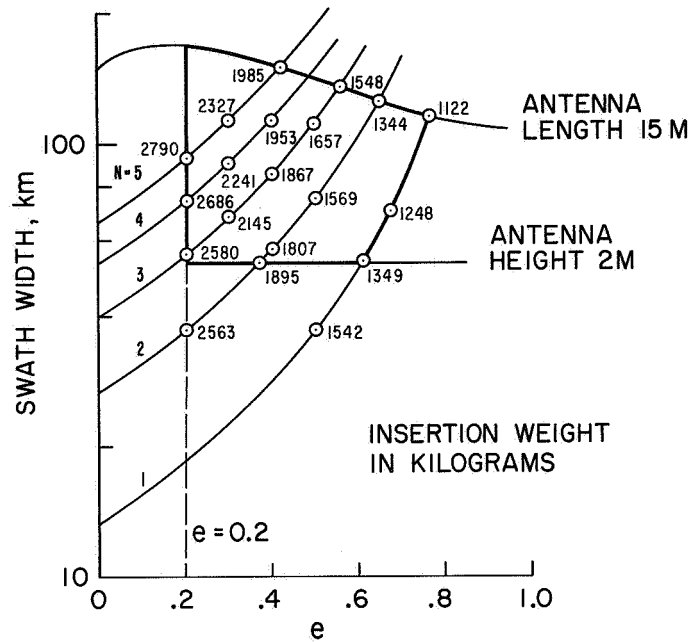


Figure 29.- Effect of operational envelope on spacecraft insertion weight;
 $H_p = 500$ km, $\lambda = 13$ cm, $\alpha = 60^\circ$, $\Lambda_{\max} = 60^\circ$.

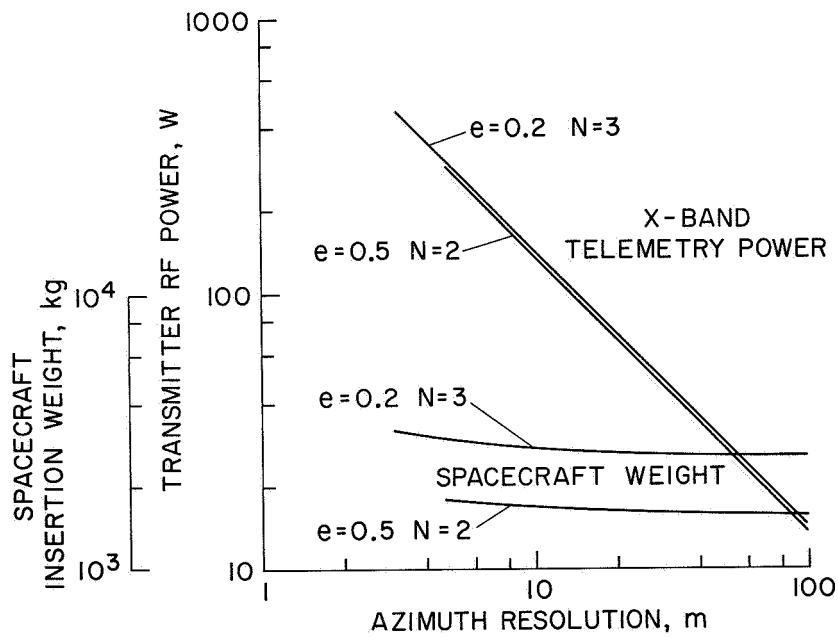


Figure 30.- Effect of dual resolution.

NATIONAL AERONAUTICS AND SPACE ADMINISTRATION
WASHINGTON, D.C. 20546

OFFICIAL BUSINESS
PENALTY FOR PRIVATE USE \$300

SPECIAL FOURTH-CLASS RATE
BOOK

POSTAGE AND FEES PAID
NATIONAL AERONAUTICS AND
SPACE ADMINISTRATION
491



POSTMASTER:

If Undeliverable (Section 158
Postal Manual) Do Not Return

"The aeronautical and space activities of the United States shall be conducted so as to contribute . . . to the expansion of human knowledge of phenomena in the atmosphere and space. The Administration shall provide for the widest practicable and appropriate dissemination of information concerning its activities and the results thereof."

—NATIONAL AERONAUTICS AND SPACE ACT OF 1958

NASA SCIENTIFIC AND TECHNICAL PUBLICATIONS

TECHNICAL REPORTS: Scientific and technical information considered important, complete, and a lasting contribution to existing knowledge.

TECHNICAL NOTES: Information less broad in scope but nevertheless of importance as a contribution to existing knowledge.

TECHNICAL MEMORANDUMS: Information receiving limited distribution because of preliminary data, security classification, or other reasons. Also includes conference proceedings with either limited or unlimited distribution.

CONTRACTOR REPORTS: Scientific and technical information generated under a NASA contract or grant and considered an important contribution to existing knowledge.

TECHNICAL TRANSLATIONS: Information published in a foreign language considered to merit NASA distribution in English.

SPECIAL PUBLICATIONS: Information derived from or of value to NASA activities. Publications include final reports of major projects, monographs, data compilations, handbooks, sourcebooks, and special bibliographies.

TECHNOLOGY UTILIZATION PUBLICATIONS: Information on technology used by NASA that may be of particular interest in commercial and other non-aerospace applications. Publications include Tech Briefs, Technology Utilization Reports and Technology Surveys.

Details on the availability of these publications may be obtained from:

SCIENTIFIC AND TECHNICAL INFORMATION OFFICE

NATIONAL AERONAUTICS AND SPACE ADMINISTRATION

Washington, D.C. 20546